

Automated deterministic full design of tensor metasurfaces for field manipulation

*Original*

Automated deterministic full design of tensor metasurfaces for field manipulation / Teodorani, Lucia; Zucchi, Marcello; Vecchi, Giuseppe. - In: IEEE TRANSACTIONS ON ANTENNAS AND PROPAGATION. - ISSN 0018-926X. - (2026).  
[10.1109/tap.2026.3687722]

*Availability:*

This version is available at: 11583/3010791 since: 2026-05-13T10:20:15Z

*Publisher:*

IEEE

*Published*

DOI:10.1109/tap.2026.3687722

*Terms of use:*

This article is made available under terms and conditions as specified in the corresponding bibliographic description in the repository

*Publisher copyright*

IEEE postprint/Author's Accepted Manuscript

©2026 IEEE. Personal use of this material is permitted. Permission from IEEE must be obtained for all other uses, in any current or future media, including reprinting/republishing this material for advertising or promotional purposes, creating new collecting works, for resale or lists, or reuse of any copyrighted component of this work in other works.

(Article begins on next page)

# Automated Deterministic Full Design of Tensor Metasurfaces for Field Manipulation

Lucia Teodorani, *Member, IEEE*, Marcello Zucchi, *Member, IEEE*, and Giuseppe Vecchi, *Life Fellow, IEEE*

**Abstract**—We present an automatic, deterministic procedure for the complete design of tensor metasurfaces, fulfilling field manipulation specifications and physical realizability constraints. Radiated field specifications are of the mask-type (inequalities). The tensor impedance pattern has full spatial variability in two dimensions, without any assumption on the tensor components or spatial variation envelope, yielding maximum flexibility. In particular, the choice of purely capacitive (or inductive) tensor impedances can be enforced. A compact representation of the impedance tensors allows to set independent bounds on the tensor components derivable from the chosen unit cell database: this ensures the synthesis of practically realizable structures. The design is based on the integral-equation formulation with a current-only approach, in which the tensor impedance profile is derived only after the optimal current is found; this allows to avoid the solution of the forward problem at all steps of the algorithm, with a drastic reduction of computational resources. 3-D metallic feeding structures are self-consistently accounted for in the design process (when present). An innovative process to optimally realize the whole set of unit cells is also described that allows to implement the full design without even computing the impedance distribution. Application examples address center-fed circular metasurface antennas, for broadside pencil beam and shaped cosecant beam with linear polarizations, and a rectangular metasurface operating as an anomalous reflector. In all cases, the design is carried out up to the final layout, and the full structure is simulated to verify the design. The method to enforce design bounds, and the impedance-free unit cell design can also be employed in design methods which are not current-based.

**Index Terms**—Impedance boundary conditions, Integral equations, Metasurface antennas, Method of moments, Optimization, Tensor metasurface.

## I. INTRODUCTION

**M**ETASURFACES (MTSs) are planar structures composed of sub-wavelength elements, that possess the ability to manipulate electromagnetic fields with high flexibility. They can be easily implemented with metallic patches of various shapes printed on dielectric substrates, and have been used to build a variety of components such as antennas [1]–[3], lenses [4]–[6], beam-forming networks [7], [8], and

most recently passive electromagnetic skins [9], [10]. Great effort has been dedicated over the years to the development of efficient design methods that, starting from application-dependent requirements, such as the desired far-field pattern for an antenna, could output the layout of the metasurface exerting this electromagnetic behavior. Since MTSs are usually very large in terms of wavelength, but composed of electrically small elements, their design is typically tackled as a two-step process: first, the local electromagnetic behavior of the surface is approximated through a single parameter – the surface impedance – using the Impedance Boundary Condition (IBC), whose unknown spatial distribution must be determined by the design; then, the impedance is locally implemented by means of properly-shaped unit cells. Well-consolidated methods are available that allow to link impedance values to specific unit cell geometries [11], thus taking care of the second stage of the MTS design process. Our work deals mostly with the first step of MTS design, specifically the synthesis of *tensor* impedances; in addition, a new method to select the unit cells is proposed.

Finally, we observe that tensor MTSs offer more flexibility in the manipulation of electromagnetic waves with respect to their scalar counterpart, thanks to the higher number of degrees of freedom [12].

### A. State of the Art

The methods for the synthesis of MTSs available in literature can be categorized as “2-D”, when one spatial coordinate is invariant or periodic in the design, or “3-D”, when full spatial variability is considered. They can be further distinguished based on the metasurface electromagnetic quantity that they try to optimize – electric field, impedance, surface current, or a combination of these; the analytical or numerical nature of this synthesis; and whether deterministic or meta-heuristic algorithms are employed.

1) *Two-Dimensional Methods*: Among 2-D methods, there is vast literature exploring analytical and numerical approaches aimed at the synthesis of metasurface-based leaky-wave antennas with a desired radiation pattern. In [13]–[15], passivity and losslessness of the synthesized metasurfaces are achieved by introducing auxiliary and evanescent surface wave fields. In [16]–[18], the metasurface design is done numerically in two steps: first, a complex-valued impedance surface is obtained from pattern-matching requirements; then, a gradient descent optimization reduces the complex impedances to purely reactive values. In [19], a dual optimization approach considering equivalent currents and impedance at the same time is employed, thus requiring the solution of the forward problem at

Manuscript received \*\*\*\*\*; revised \*\*\*\*\*. This work was supported by the European Union - Next Generation EU through Italian National Recovery and Resilience Plan (NRRP), Mission 4, Component 2, Investment 1.3, partnership on “Telecommunications of the Future” - PE00000001 RE-Search and innovation on future Telecommunications systems and networks, to make Italy more smART (RESTART) - under Grant CUP E13C22001870001. (*Corresponding author: Lucia Teodorani*).

L. Teodorani and G. Vecchi are with the Department of Electronics and Telecommunications, Politecnico di Torino, Turin 10129, Italy (e-mail: lucia.teodorani@polito.it; giuseppe.vecchi@polito.it). M. Zucchi is with the Advanced Computing, Photonics and Electromagnetics (CPE) Area, Fondazione LINKS, 10138 Turin, Italy (e-mail: marcello.zucchi@linksfoundation.com).

each step. Conversely, a current-only design method is adopted in [20], where the resulting non-convex problem is approached with a global optimizer; the same approach is employed in [21] with a gradient-based optimization.

2) *Three-Dimensional Methods*: The design of 3-D varying metasurfaces has been initially based on wave physics and analytical considerations, e.g., [1], [2]; these approaches are tailored to (locally) sinusoidally modulated MTS antennas, that require specific parameterizations and cannot accommodate for arbitrary design specifications. In [12], an aperture synthesis approach based on local holography and variable impedance modulation is described. In [22], the design of tensor metasurfaces transforming an incident wave into arbitrarily specified reflected and refracted waves is tackled using susceptibility tensors, yielding closed-form solutions.

As for numerical methods, the works in [23]–[26] are of the current-only type and can synthesize both scalar and tensor metasurfaces, starting from a target field to be specified in amplitude and phase. The work in [27] is an impedance-based optimization, that employ a physics-based specialized parametric impedance profile. In [7], the forward problem is tackled in terms of a 2-D circuit network solver by using reduced-order models of the metasurface unit cells. The work in [28] extends the 2-D two-step method of [18] to the synthesis of 3-D metasurfaces. In [29], reflectarray design is addressed by defining analytical closed-form expressions for the computation of the surface currents that radiate a desired far-field pattern and exploiting nonradiating currents to ensure compliance with user-defined geometrical constraints. This approach is generalized in [30] to deal with non-analytical synthesis problems with nonlinear constraints by employing a particle swarm-inspired optimization. In [31], metasurface synthesis enabled by global optimization is made computationally feasible by using specialized entire-domain basis functions.

## B. Innovation

We present an automatic, deterministic procedure for the complete design of tensor metasurfaces. Field manipulation specifications accommodate mask-type (inequalities) requirements, and the tensor impedance pattern has full spatial variability in two dimensions, without any assumption on the tensor components or spatial variation envelope. The design goes all the way down to unit cell design, and the method incorporates realizability bounds on the tensor components derivable from the chosen unit cell database: this ensures the synthesis of practically realizable structures. Design instances run on a standard desktop PC in a few hours for surfaces of tens of wavelengths across. To the best of the authors' knowledge this is entirely new with respect to the present literature.

More specifically, we start from the automated method for the design of metasurfaces described in [32], [33], initially developed to deal with scalar impedances. Here, we achieve the synthesis of tensor surfaces, keeping the same extreme computational efficiency. The key innovations that have enabled this achievement are:

- 1) the closed-form retrieval of the impedance tensor in terms of the optimized current;

- 2) the formulation of the impedance realizability constraints, allowing to enforce in the first place the synthesis of a purely capacitive surface (or inductive, if desired).

As mentioned before, a current-based automated method has the advantage of not requiring the solution of the forward problem at each iteration of the optimization process. For this to be possible, all impedance realizability constraints must be formulated in terms of the surface current only. Therefore, differently from the isotropic version of the algorithm presented in [32], [33], new strategies are needed to uniquely retrieve the tensor impedance components from the surface current and to enforce the feasibility constraints without explicitly computing these quantities.

One of main issues in synthesizing tensor impedances is the very definition of physical realizability, beyond the requirement of passivity and losslessness. In fact, considering a database of synthesizable anti-Hermitian and reciprocal tensors, where each entry is characterized by three impedance components, the imposition of fixed, *independent* upper and lower bounds on each component over the whole metasurface would not guarantee that the resulting impedance tensor is actually realizable (i.e., that it corresponds to a database entry). Even more fundamentally, it is not obvious to enforce a fully capacitive (or inductive) surface. The method described in this work resolves this issue by enforcing realizability bounds on the *eigenvalues* of the impedance tensor (specifically, on their isotropic and anisotropic components): it will be shown that this strategy allows to identify a region of feasibility, with bounds expressed as at most second-order polynomial functions of two quantities only, inside of which each parameter combination corresponds to a realizable impedance tensor.

In another radical departure from the state of the art, a new technique is introduced to select the proper unit cells for implementing the designed surface from a standard precomputed database. This method employs only the current and associated (electric) field, and does not require the determination of the (tensor) impedance profile from the optimal current; this approach will be referred to as “field matching”.

Both the above field matching unit-cell design and the method to assess tensor realizability bounds can be directly employed in other approaches, whether they are of current-only type [20], [21], [23], [24], or based on the global optimization of the impedance profile [1], [2], [27], [31].

## C. Summary of Capabilities

This paper, taken together with the previous works [32], [33], constitutes a systematic design method with the capabilities listed below.

- It allows mask-type (inequality) field specifications; at present, it is the only current-based method with this ability. This allows its use in practical design instances with requirements of compliance with sidelobe (SL) masks (e.g., ITU, ETSI) and gain maximization (if so required).
- It is completely agnostic: it does not require any information on the targeted wave phenomena (e.g. leaky waves), and no parametrization of the impedance profile.

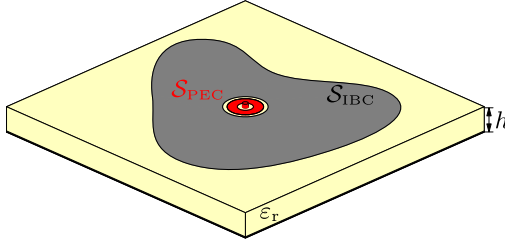


Fig. 1. Reference geometry for the tensor metasurface antenna.

- The process optimizes the *realized* gain. This optimization intrinsically minimizes reflection from the metasurface, and the residual surface wave guided in the dielectric – and hence its diffraction at the rim. An example of this, with comparison with 3-D commercial solver simulations and measurements can be found in [34].
- It allows to include the effect of the feeding structure into the metasurface design; at present, it is the only current-based method with this ability.
- It is solve-free, like other current-only methods: no solution of the forward problem (“simulation”) is required at any iteration.
- It allows the specification of tensor impedance constraints. This is unique to the present approach, but applicable to all design methods.

Very preliminary results relative to the present work have been presented in conference papers [35], [36]; this is the first account of the method and its implementation.

This paper is organized as follows. Section II illustrates the framework of the current-only design method, while Section III defines the concept of realizable tensor impedance. Section IV introduces the technique to retrieve the tensor impedance components from the surface current, while Section V shows how to enforce the proper realizability constraints. A new strategy to optimally select unit cells from a database is described in Section VI. The proposed method is applied to four design cases and the results are reported in Section VII. Finally, conclusions are drawn in Section VIII.

## II. BACKGROUND

In this Section, the current-based automated method for the synthesis of metasurface antennas, described in detail in [32], [33], [37], is summarized for convenience.

### A. Forward Problem

The reference geometry for the metasurface antenna is shown in Fig. 1. The antenna geometry is divided in two regions, coherently with what was done in [33]: the Impedance Boundary Condition (IBC) region is the area on which the unknown tensor impedance must be determined, while the PEC region corresponds to the feeding structure elements (central pin and annular ring). The electromagnetic problem is formulated as an *Electric Field Integral Equation*:

$$[\mathbf{E}_{\text{inc}}(\mathbf{r}) + \mathcal{L}\mathbf{J}(\mathbf{r})]_{\text{tan}} = \begin{cases} \overline{\overline{\mathbf{Z}}}(\mathbf{r}) \cdot \mathbf{J}(\mathbf{r}), & \mathbf{r} \in \mathcal{S}_{\text{IBC}} \\ \mathbf{0}, & \mathbf{r} \in \mathcal{S}_{\text{PEC}} \end{cases} \quad (1)$$

where  $\mathbf{J}$  is the equivalent current density,  $\mathbf{E}_{\text{inc}}$  is the incident field generated by the sources in the absence of the metasurface and all metallic (PEC) parts,  $\overline{\overline{\mathbf{Z}}}$  is the surface impedance tensor, and  $\mathcal{L}$  is the *Electric Field Integral Operator* (EFIO) defined as

$$\mathcal{L}\mathbf{J}(\mathbf{r}) = \iint \overline{\overline{\mathbf{G}}}^{\text{EJ}}(\mathbf{r}, \mathbf{r}') \cdot \mathbf{J}(\mathbf{r}') dS(\mathbf{r}'). \quad (2)$$

In the above,  $\overline{\overline{\mathbf{G}}}^{\text{EJ}}$  is the multilayer dyadic Green’s function for the (grounded or ungrounded) substrate [38].

The usual Method of Moments approach with Galerkin testing and Rao-Wilton-Glisson (RWG) basis functions  $\Lambda_n$  [39] is used to discretize the forward problem (1).

We further express the impedance tensor  $\overline{\overline{\mathbf{Z}}}(\mathbf{r})$  in terms of  $L$  tensor basis functions  $\overline{\overline{\psi}}_l(\mathbf{r})$  (yet to be specified),

$$\overline{\overline{\mathbf{Z}}}(\mathbf{r}) = \sum_{l=1}^L Z_l \overline{\overline{\psi}}_l(\mathbf{r}), \quad (3)$$

and with this the forward problem reduces to the linear system

$$\mathbf{V}_{\text{inc}} + \mathbf{L}\mathbf{l} = \mathbf{Z}\mathbf{l}, \quad (4)$$

where the array  $\mathbf{l}$  collects the RWG basis coefficients  $I_n$  and the remaining quantities are defined as

$$(\mathbf{L})_{mn} = \langle \Lambda_m, \mathcal{L}\Lambda_n \rangle, \quad (5)$$

$$(\mathbf{Z})_{mn} = \sum_{l=1}^L Z_l \langle \Lambda_m, \overline{\overline{\psi}}_l \cdot \Lambda_n \rangle, \quad (6)$$

$$(\mathbf{V}_{\text{inc}})_m = \langle \Lambda_m, \mathbf{E}_{\text{inc}} \rangle. \quad (7)$$

In the above,  $\langle \mathbf{a}, \mathbf{b} \rangle$  indicates the symmetric bilinear form

$$\langle \mathbf{a}, \mathbf{b} \rangle = \frac{1}{A_\Sigma} \int_\Sigma \mathbf{a} \cdot \mathbf{b} dS, \quad (8)$$

where  $\Sigma$  is a surface of interest (e.g., of the mesh cell), and  $A_\Sigma$  is its area. It is understood from (1) that, for basis functions that lie on  $\mathcal{S}_{\text{PEC}}$ , the matrix entries (6) are equal to zero.

Finally, the far-field can be computed from the current via the *radiation operator*  $\mathcal{R}$ :

$$\mathcal{R}\mathbf{J}(\hat{\mathbf{r}}) = \frac{k_0}{2\pi j} \iint \overline{\overline{\mathbf{G}}}^{\text{ff}}(\hat{\mathbf{r}}, \mathbf{r}') \cdot \mathbf{J}(\mathbf{r}') dS(\mathbf{r}') \quad (9)$$

where  $\overline{\overline{\mathbf{G}}}^{\text{ff}}(\hat{\mathbf{r}}, \mathbf{r}')$  is the multilayer far-field tensor [40] and the unit vector  $\hat{\mathbf{r}}(\theta, \varphi)$  identifies the direction of radiation in spherical coordinates.

### B. Current-Based Inverse Design

The goal of the design process is the synthesis of an impedance profile that, for a given incident field and feeding structure (if present), radiates a far-field pattern obeying mask-type specifications and is physically feasible, i.e., locally passive, lossless and implementable with printed metallic elements.

In the current-only numerical method for the synthesis of metasurfaces described in [32], [33], [37], the total cost function that the algorithm aims to minimize can be expressed as

$$f = f_{\text{rad}} + f_{\text{ibc}} + f_{\text{pec}}, \quad (10)$$

where each term is a functional, i.e., a scalar-valued non-negative function of the surface current *only*. Here,  $f_{\text{rad}}$  accounts for the radiated field requirements,  $f_{\text{ibc}}$  encompasses the realizability constraints to be enforced on the IBC region, and  $f_{\text{pec}}$  represents the PEC condition on the related surface.

For the minimization of the cost function a *nonlinear conjugate gradient* algorithm [41, p. 121] is employed, as done in [32], [33]; all operations are cast in such a way to be amenable to the use of fast factorizations, with  $O(N)$  memory requirements and  $O(N \log N)$  complexity per iteration.

### III. TENSOR IMPEDANCE AND REALIZABILITY

#### A. Tensor IBC Requirements

The radiated field and PEC terms, introduced in [32], [33], are reported in Appendices A and B for convenience. Differently from the isotropic version of the method presented in the aforementioned works, the IBC realizability functional  $f_{\text{ibc}}$  must now be tailored to the synthesis of tensor impedances.

In order to implement a current-only method for the synthesis of tensor metasurfaces, three fundamental issues must be addressed:

- the definition of physical realizability for a tensor impedance,
- the extraction of tensor impedance components from the surface current and electric field, and
- the imposition of the physical realizability constraints in terms of the current coefficients only.

The issue of how to define the bounds for physical realizability on a tensor impedance surface arises from the interdependence of these bounds between the components of the impedance tensor. For reciprocal and lossless unit cells, the impedance tensor is characterized by three independent components: imposing upper and lower bounds separately on these terms does not guarantee that the resulting combination corresponds to a realizable tensor. In this work, this problem is tackled by considering the *eigenvalues* of the impedance tensor: the signs of these quantities are indicative of the capacitive or inductive behavior of the unit cell, and from their expressions it is possible to define feasibility bounds on two quantities only. This will be shown in reference to a realistic unit cell geometry in Section III-B.

As for the derivation of the tensor impedance components from the surface current and electric field, this is achieved by employing a new testing strategy that generalizes the scalar impedance retrieval technique described in [32], [37]. This will be explained in Section IV.

Finally, in order to fully benefit from the computational advantages of a current-based design method, the feasibility constraints are expressed in such a way that the resulting functionals are fourth-degree multivariate polynomials in the current coefficients, thus allowing to perform a closed-form line search procedure in the nonlinear conjugate gradient algorithm [32], [33]. These functionals will be described in detail in Section V.

#### B. Impedance Tensor Representation and Realizability

A general tensor impedance can be expressed as a linear combination of four basis dyadics (not to be confused with the spatial tensor basis functions  $\overline{\overline{\psi}}_l(\mathbf{r})$  in (3)) [37], [42]:

$$\overline{\overline{\mathbf{Z}}} = Z_I \overline{\overline{\mathbf{I}}} + Z_N \overline{\overline{\mathbf{N}}} + Z_K \overline{\overline{\mathbf{K}}} + Z_L \overline{\overline{\mathbf{L}}}, \quad (11)$$

whose expressions in terms of a local orthonormal basis  $(\hat{\mathbf{u}}, \hat{\mathbf{v}})$  are given by

$$\overline{\overline{\mathbf{I}}} = \hat{\mathbf{u}}\hat{\mathbf{u}} + \hat{\mathbf{v}}\hat{\mathbf{v}}, \quad (12)$$

$$\overline{\overline{\mathbf{N}}} = \hat{\mathbf{v}}\hat{\mathbf{u}} - \hat{\mathbf{u}}\hat{\mathbf{v}}, \quad (13)$$

$$\overline{\overline{\mathbf{K}}} = \hat{\mathbf{u}}\hat{\mathbf{u}} - \hat{\mathbf{v}}\hat{\mathbf{v}}, \quad (14)$$

$$\overline{\overline{\mathbf{L}}} = \hat{\mathbf{v}}\hat{\mathbf{u}} + \hat{\mathbf{u}}\hat{\mathbf{v}}. \quad (15)$$

As explained in [37], [42], the condition of *passivity* and *losslessness* for a tensor impedance requires

$$\text{Re } Z_I = \text{Im } Z_N = \text{Re } Z_K = \text{Re } Z_L = 0. \quad (16)$$

In addition, the condition  $\text{Re } Z_N = 0$  is enforced. This is done because the term  $\text{Re } Z_N$  implies an in-phase transfer of energy from one polarization to the other, which is typically achieved by resonant unit cells that exhibit a bianisotropic behavior (e.g., split ring or omega particle); however, the use of these geometries complicates the layout design and is outside the scope of this work. Consequently, only unit cells with  $\text{Re } Z_N = 0$  will be considered. Therefore, the expression of a passive and lossless tensor impedance becomes

$$\overline{\overline{\mathbf{Z}}} = jX_I \overline{\overline{\mathbf{I}}} + jX_K \overline{\overline{\mathbf{K}}} + jX_L \overline{\overline{\mathbf{L}}}. \quad (17)$$

In matrix form, the impedance tensor can be written as

$$\mathbf{Z} = j\mathbf{X} = j \begin{bmatrix} X_{uu} & X_{uv} \\ X_{vu} & X_{vv} \end{bmatrix} = j \begin{bmatrix} X_I + X_K & X_L \\ X_L & X_I - X_K \end{bmatrix}. \quad (18)$$

It is clear that  $X_I$  represents the isotropic component of the impedance tensor, while  $X_K$  and  $X_L$  account for the anisotropy. This matrix can be diagonalized as

$$\mathbf{Z} = j\mathbf{R}(\xi)\mathbf{X}^d\mathbf{R}^T(\xi), \quad (19)$$

where

$$\mathbf{X}^d = \begin{bmatrix} X_1 & 0 \\ 0 & X_2 \end{bmatrix} \quad (20)$$

is the eigenvalues matrix (with  $X_1 \geq X_2$ ), and

$$\mathbf{R}(\xi) = \begin{bmatrix} \cos \xi & -\sin \xi \\ \sin \xi & \cos \xi \end{bmatrix} \quad (21)$$

is a rotation matrix of an angle  $\xi$ , formed by the eigenvector corresponding to the eigenvalue  $X_1$  with the  $x$ -axis. The eigenvalues  $X_1$  and  $X_2$  can be computed as

$$X_1 = X_I + X_A, \quad (22)$$

$$X_2 = X_I - X_A, \quad (23)$$

with

$$X_A = \sqrt{X_K^2 + X_L^2} \quad (24)$$

representing the *magnitude* of the anisotropic part of the tensor, while the angle parameter  $\xi$  is given by

$$\xi = \text{atan2}(X_L, X_K)/2 \quad (25)$$

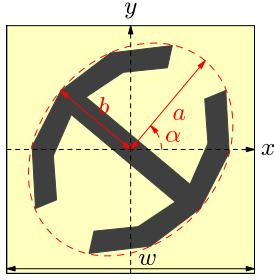


Fig. 2. Reference layout of the double-anchor unit cell.

where  $\text{atan2}$  is the four-quadrant inverse tangent function.

The fundamental control that in practice one needs is over the surface impedance being capacitive or inductive, with capacitive being the usual requirements for metasurfaces based on textures of metallic patches. The capacitive or inductive reactance needs to be related to its original physical meaning, i.e., it must be interpreted in terms of the (surface density of the) stored energy appearing in Poynting's theorem (see also [32]):

$$w_e = \text{Im}(\mathbf{E}_{\text{tan}} \cdot \mathbf{J}^*), \quad (26)$$

with capacitive implying negative sign, i.e.,  $w_e < 0$  (with the  $e^{j\omega t}$  convention) and positive for inductive. As shown in App. C, the capacitive or inductive behavior is expressed by the sign of the eigenvalues  $X_1, X_2$ ; in particular, a capacitive reactance requires that *both* eigenvalues  $X_1, X_2$  be negative, and vice-versa for inductive.

Hence, considering that by definition (24),  $X_A \geq 0$ , the most usual capacitive choice requires

$$X_I < -X_A, \quad (27)$$

or, equivalently,

$$X_I < 0, \quad (28)$$

$$X_I^2 > X_A^2. \quad (29)$$

These are the conditions to enforce to ensure that the synthesized impedance profile be realizable with capacitive unit cells. The condition  $X_I < 0$  is intuitive, while  $X_I^2 > X_A^2$  indicates that the isotropic part must dominate on the anisotropic one, thus yielding a relevant cell design criterion.

It appears evident that the three impedance tensor entries  $X_I, X_K, X_L$  can be equivalently substituted by the three terms  $X_I, X_A, \xi$ ; however, the fundamental capacitive (or inductive) condition involves *only* the relation between the isotropic part  $X_I$  and the anisotropic component  $X_A$ .

Furthermore, the automated design process can be enhanced to achieve realizability by constraining impedance tensors to belong to the set of those available for a given unit cell geometry and materials. This is an endeavor of clear practical relevance, and can be useful to all methods that are based on the separation of the design process into impedance profile synthesis and subsequent unit cell implementation; in particular, it applies to both meta-heuristic [30] and analytic-based designs [2].

In order to make the ensuing discussion clearer, we introduce the unit cell types that will be used throughout the

applications in Section VII. The geometry is that of a double-anchor, as shown in Fig. 2, that was first introduced in [3]; two different unit cell databases are considered at a frequency of 23 GHz, printed on a RO3003 dielectric substrate with  $\epsilon_r = 3$  and thickness 1.27 mm: one has a periodicity  $w$  equal to 1.625 mm ( $\lambda_0/8$ ), and the other 2.6 mm ( $\lambda_0/5$ ). The varying parameters are the lengths of the major and minor semi-axes  $a$  and  $b$  and the rotation angle  $\alpha$  with respect to the  $x$ -axis of the global reference frame. Employing the technique described in [11], one can compute the sheet impedance tensor for every possible combination of these parameters, thus populating the tensor impedance sets to be used for the unit cell design. Assuming  $(\hat{u}, \hat{v}) = (\hat{x}, \hat{y})$ , the quantities  $X_I, X_K, X_L$  and the eigenvalues  $X_1, X_2$  can be retrieved using (18), (22), (23) for every entry of the impedance databases.

The realizable set  $\mathcal{P}$  in the parameter space  $\mathbf{p} = (p_1, \dots, p_M)$  (here  $(a, b, \alpha)$ ) is typically the hypercube obtained by Cartesian products of the allowed variability intervals  $\mathcal{I}_m = [p_m^{\min}, p_m^{\max}]$ , i.e.,  $\mathcal{P} = \mathcal{I}_1 \times \dots \times \mathcal{I}_M$ . Each parameter array  $\mathbf{p}$  maps into one impedance tensor,

$$\mathbf{p} \mapsto \mathbf{j}\mathbf{X}(\mathbf{p}), \quad (30)$$

and the realizable parameter set  $\mathcal{P}$  maps into the realizability set  $\mathcal{X}$  for the impedance tensor,

$$\mathcal{P} \rightarrow \mathcal{X}. \quad (31)$$

The main difficulty of the design process arises from the fact that this mapping does not transform the parameter hypercube  $\mathcal{P}$  into an hypercube for either the local coordinates basis  $X_{uu}, X_{uv}, X_{vv}$  or the tensor basis  $X_I, X_K, X_L$ ; hence, one cannot simply impose the realizability constraints on the impedance tensor components *separately*.

For most types of practical unit cells, this issue is eased using the eigenvalue representation described above. The typical unit cells have one or two symmetry planes (such as the double-anchor in Fig. 2), and the rotation ( $\alpha$  here) is one of the design parameters; in this case, it turns out that the mapping between the geometrical cell rotation  $\alpha$  and the ‘‘spectral’’ rotation angle  $\xi$  in (21) is a dense continuous mapping. This is obvious if one considers the cell in isolation, and remains true also in a periodic environment. Hence, any ratio between the two anisotropic components  $X_L$  and  $X_K$  (see (25)) can be accommodated in any data set by choosing a suitable rotation angle, and one can concentrate the feasibility study on the two parameters  $X_I$  and  $X_A$  that are solely responsible for the fundamental capacitive or inductive property of the cell.

Figure 3 shows all database entries for the unit cell with periodicity  $\lambda_0/8$ , obtained by uniform sampling of the parameter space, as points in the plane  $(X_I, X_A)$ : it can be seen that all the tensor impedance values are found below the line  $X_A = -X_I$ , thus characterizing this database as fully capacitive (see (27)). Conversely, if the same plot is produced for the tensor impedance database of the larger double-anchor unit cell with periodicity equal to  $\lambda_0/5$  (see Fig. 4), one can observe that there are several points in the plane  $(X_I, X_A)$  within the region defined by  $X_A \geq |X_I|$ , with some values characterized by  $X_I > 0$ . These points correspond to impedance tensors having one negative and one positive

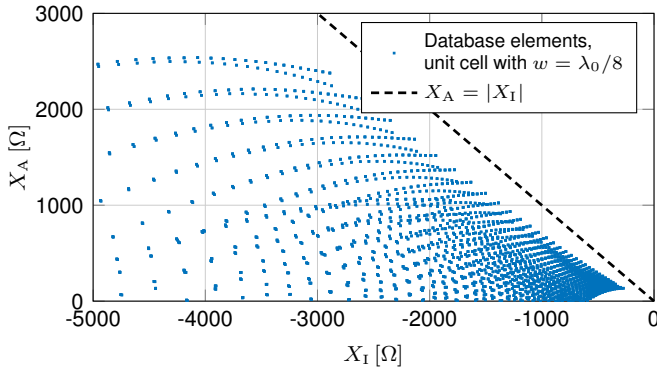


Fig. 3. Relation between the anisotropic tensor component  $X_A$  and the isotropic tensor component  $X_I$  for the impedance database of a double-anchor unit cell with periodicity  $w = \lambda_0/8$ ; the dots represent computed entries of the database.

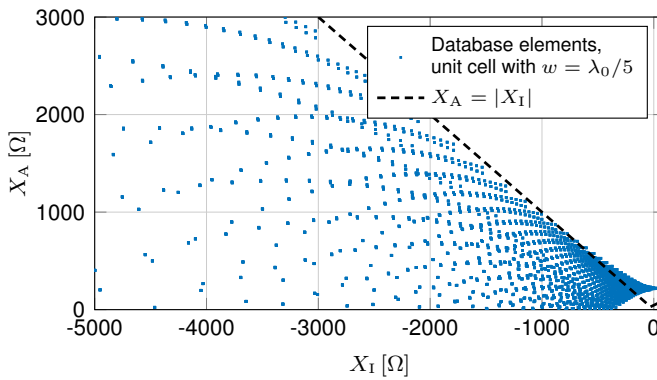


Fig. 4. Relation between the anisotropic tensor component  $X_A$  and the isotropic tensor component  $X_I$  for the impedance database of a double-anchor unit cell with periodicity  $w = \lambda_0/5$ ; the dots represent computed entries of the database.

eigenvalue between  $X_1$  and  $X_2$ , with a mixed capacitive and inductive behavior.

The issue remains of the proper definition and enforcement of the realizability constraints, with reference to the specific unit cell database; while it is paramount that the impedance variability range of the isotropic component  $X_I$  be enforced keeping track of the proper negative or positive sign, it would be easier to deal with the square of the anisotropic part  $X_A$ , to get rid of the square root function in the expression of the realizability functionals. To this aim, the same database entries of Figs. 3 and 4 are now plotted in the plane  $(X_I, X_A^2)$ , as shown in Figs. 5 and 6.

The appropriate feasibility constraints to be imposed in the current-based synthesis process can be properly identified on the basis that these constraints must be at most quadratic in the domain given by  $(X_I, X_A^2)$ : the proposed optimization algorithm relies, for computational efficiency, on the formulation of the objective functionals as at most fourth-degree polynomials in the current coefficients, and parabolic constraints in terms of the abscissa  $X_I$  and ordinate  $X_A^2$  do translate into functionals with the aforementioned properties, as will be explained in Section V. Based on these considerations, the impedance realizability constraints are set as follows:

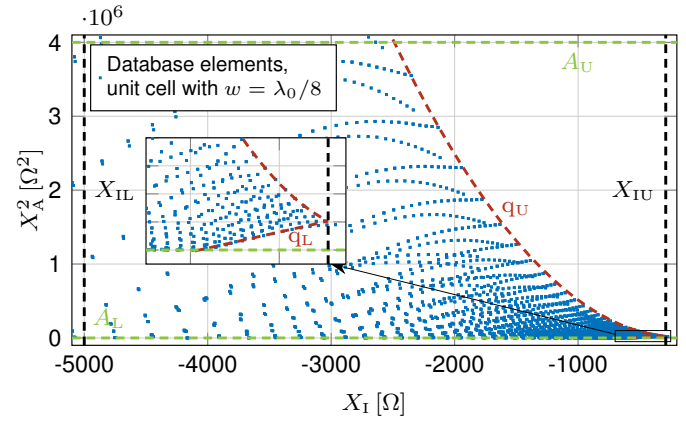


Fig. 5. Impedance database entries for the double-anchor unit cell with periodicity  $w = \lambda_0/8$  represented as points in the plane  $(X_I, X_A^2)$ . The dashed lines indicate the constraints that will be enforced in the design to ensure feasibility. The inset shows a zoomed view of a densely populated area.

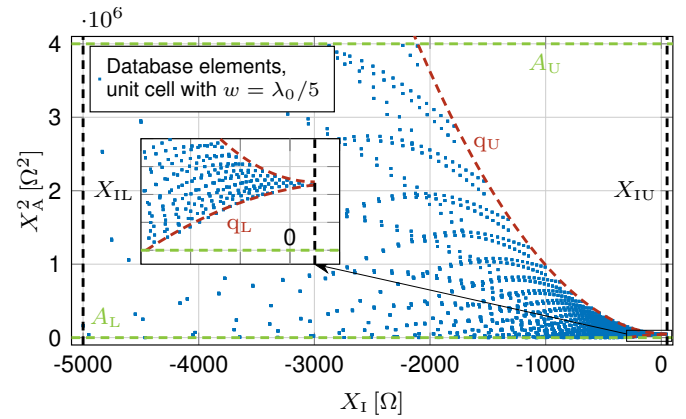


Fig. 6. Impedance database entries for the double-anchor unit cell with periodicity  $w = \lambda_0/5$  represented as points in the plane  $(X_I, X_A^2)$ . The dashed lines indicate the constraints that will be enforced in the design to ensure feasibility. The inset shows a zoomed view of a densely populated area.

- Upper ( $X_{IU}$ ) and lower ( $X_{IL}$ ) bounds are imposed on the isotropic component  $X_I$ ; these bounds are represented by the vertical dashed lines in Figs. 5 and 6 and their insets.
- Upper ( $A_U$ ) and lower ( $A_L$ ) bounds are set on the *square* of the anisotropic part  $X_A^2$ ; these bounds are represented by the horizontal dashed lines in Figs. 5 and 6 and their insets.
- Finally, the feasibility region is delimited by two additional constraints, corresponding to two parabolas with equations in the plane  $(x, y) \equiv (X_I, X_A^2)$  given by  $q_U : y = a_U x^2 + b_U x + c_U$  and  $q_L : y = a_L x^2 + b_L x + c_L$  (see Figs. 5 and 6). From the inset in Fig. 5 it can be seen that these constraints can be easily reduced to straight lines by setting  $a_{U,L} = 0$ .

These parameters, for the considered databases of Figs. 5 and 6, are summarized in Table I. They are obtained by fitting the boundaries of the cluster of database points with the functions described before. The enforcement of these feasibility constraints, based on the expression of the tensor

TABLE I  
PARAMETERS APPEARING IN THE TENSOR IMPEDANCE CONSTRAINTS,  
FOR THE DATABASES OF FIGS. 5 AND 6.

| $w$      | $\lambda_0/8$      | $\lambda_0/5$      |
|----------|--------------------|--------------------|
| $X_{IU}$ | $-290 \Omega$      | $50 \Omega$        |
| $X_{IL}$ | $-5000 \Omega$     | $-5000 \Omega$     |
| $A_U$    | $4000000 \Omega^2$ | $4000000 \Omega^2$ |
| $A_L$    | $20 \Omega^2$      | $0.3 \Omega^2$     |
| $a_U$    | $0.75$             | $0.85$             |
| $b_U$    | $273.4 \Omega$     | $-85 \Omega$       |
| $c_U$    | $36790 \Omega^2$   | $51125 \Omega^2$   |
| $a_L$    | $0$                | $-0.28$            |
| $b_L$    | $71 \Omega$        | $71 \Omega$        |
| $c_L$    | $41200 \Omega^2$   | $43997 \Omega^2$   |

impedance components in terms of surface current and electric field, will be explained in Section V.

#### IV. RETRIEVAL OF THE TENSOR IMPEDANCE FROM THE SURFACE CURRENT

Once the optimal surface current has been found through the optimization procedure, a new testing strategy must be devised in order to extract all the relevant components of the impedance tensor from the knowledge of the surface current and electric field. Considering the expression of a realizable tensor impedance (17), mimicking the approach used in [32], [37], we can define the following impedance tensor basis functions:

$$\overline{\overline{\psi}}_{B_i}(\mathbf{r}) = \mathbb{I}_i(\mathbf{r}) \overline{\overline{B}} = \begin{cases} \overline{\overline{B}}, & \text{for } \mathbf{r} \in S_i \\ \overline{\overline{0}}, & \text{elsewhere} \end{cases} \quad i \in \mathcal{I}_{ibc} \quad (32)$$

where  $\mathbb{I}_i(\mathbf{r})$  is the characteristic function of each mesh triangle  $S_i \subset S_{IBC}$  (equal to 1 inside  $S_i$  and 0 outside) and  $\overline{\overline{B}}$  is any one of  $\overline{\overline{I}}$ ,  $\overline{\overline{K}}$ , or  $\overline{\overline{L}}$ . We then use a set of functions  $\tau_T(\mathbf{r})$ ,

$$\tau_{Ti}(\mathbf{r}) = \mathbb{I}_i(\mathbf{r}) \overline{\overline{T}} \cdot \mathbf{J}^*(\mathbf{r}), \quad i \in \mathcal{I}_{ibc} \quad (33)$$

where  $\overline{\overline{T}}$  is one of  $\overline{\overline{I}}$ ,  $\overline{\overline{N}}$ ,  $\overline{\overline{K}}$  or  $\overline{\overline{L}}$ , to test the general realizable IBC equation:

$$\langle \tau_T, \mathbf{E}_{\text{tan}} \rangle = \langle \tau_T, \overline{\overline{Z}} \cdot \mathbf{J} \rangle \quad (34)$$

with  $\overline{\overline{Z}} = \mathbf{j} \sum_i (X_{Ii} \overline{\overline{\psi}}_{Ii} + X_{Ki} \overline{\overline{\psi}}_{Ki} + X_{Li} \overline{\overline{\psi}}_{Li})$ . Using the multiplicative relationships between dyads (and dyadics) [43] to compute the products of pairs of tensors, and keeping in mind that  $\overline{\overline{N}}^T = -\overline{\overline{N}}$ , we obtain a set of four equations for each mesh triangle,

$$\mathbf{j}X_I \mu_I + \mathbf{j}X_K \mu_K + \mathbf{j}X_L \mu_L = S_I, \quad (35)$$

$$\mathbf{j}X_I \mu_N + \mathbf{j}X_K \mu_L - \mathbf{j}X_L \mu_K = S_N, \quad (36)$$

$$\mathbf{j}X_I \mu_K + \mathbf{j}X_K \mu_I - \mathbf{j}X_L \mu_N = S_K, \quad (37)$$

$$\mathbf{j}X_I \mu_L + \mathbf{j}X_K \mu_N + \mathbf{j}X_L \mu_I = S_L, \quad (38)$$

where the following auxiliary quantities have been defined:

$$\mu_I = \langle \mathbf{J}^*, \overline{\overline{I}} \cdot \mathbf{J} \rangle = |J_u|^2 + |J_v|^2, \quad (39)$$

$$\mu_N = \langle \mathbf{J}^*, \overline{\overline{N}} \cdot \mathbf{J} \rangle = -J_u^* J_v + J_u J_v^* = 2\mathbf{j} \text{Im}(J_u J_v^*), \quad (40)$$

$$\mu_K = \langle \mathbf{J}^*, \overline{\overline{K}} \cdot \mathbf{J} \rangle = |J_u|^2 - |J_v|^2, \quad (41)$$

$$\mu_L = \langle \mathbf{J}^*, \overline{\overline{L}} \cdot \mathbf{J} \rangle = J_u^* J_v + J_u J_v^* = 2 \text{Re}(J_u J_v^*), \quad (42)$$

$$S_I = \langle \mathbf{J}^*, \overline{\overline{I}} \cdot \mathbf{E} \rangle = J_u^* E_u + J_v^* E_v, \quad (43)$$

$$S_N = \langle \mathbf{J}^*, \overline{\overline{N}} \cdot \mathbf{E} \rangle = -J_u^* E_v + J_v^* E_u, \quad (44)$$

$$S_K = \langle \mathbf{J}^*, \overline{\overline{K}} \cdot \mathbf{E} \rangle = J_u^* E_u - J_v^* E_v, \quad (45)$$

$$S_L = \langle \mathbf{J}^*, \overline{\overline{L}} \cdot \mathbf{E} \rangle = J_u^* E_v + J_v^* E_u. \quad (46)$$

In the above,  $J_u$ ,  $J_v$  and  $E_u$ ,  $E_v$  represent the components of the surface current and tangential electric field expressed in the local basis  $(\hat{u}, \hat{v})$ , and are intended as *averages* over the mesh triangle. From (39)–(42) it can be observed that the quantities  $\mu_I$ ,  $\mu_K$  and  $\mu_L$  are real, while  $\mu_N$  is purely imaginary. Keeping this in mind, (35)–(38) can be decomposed in real and imaginary parts as follows:

$$X_I \mathcal{J}_I + X_K \mathcal{J}_K + X_L \mathcal{J}_L = Q_I, \quad (47)$$

$$0 = P_I, \quad (48)$$

$$X_K \mathcal{J}_L - X_L \mathcal{J}_K = Q_N, \quad (49)$$

$$-X_I \mathcal{J}_N = P_N, \quad (50)$$

$$X_I \mathcal{J}_K + X_K \mathcal{J}_I = Q_K, \quad (51)$$

$$X_L \mathcal{J}_N = P_K, \quad (52)$$

$$X_I \mathcal{J}_L + X_L \mathcal{J}_I = Q_L, \quad (53)$$

$$-X_K \mathcal{J}_N = P_L, \quad (54)$$

where

$$\mathcal{J}_T = \text{Re} \mu_T = \mu_T, \quad T = I, K, L, \quad (55)$$

$$\mathcal{J}_N = \text{Im} \mu_N, \quad (56)$$

$$P_T = \text{Re} S_T, \quad Q_T = \text{Im} S_T, \quad T = I, N, K, L. \quad (57)$$

In the above expressions, (48) expresses the condition of passivity and losslessness

$$\text{Re}(\mathbf{E}_{\text{tan}} \cdot \mathbf{J}^*) = 0, \quad (58)$$

which is enforced with the same functional as in [32], [33]. That being said, what remains is seven useful equations for three unknowns. This system is clearly overdetermined; a subset of equations is therefore sufficient to retrieve the three components of the impedance tensor. In particular, selecting (50), (54) and (52), a diagonal system is obtained:

$$\begin{bmatrix} -\mathcal{J}_N & 0 & 0 \\ 0 & -\mathcal{J}_N & 0 \\ 0 & 0 & \mathcal{J}_N \end{bmatrix} \begin{bmatrix} X_I \\ X_K \\ X_L \end{bmatrix} = \begin{bmatrix} P_N \\ P_L \\ P_K \end{bmatrix}. \quad (59)$$

From this, the components of the tensor can be obtained:

$$X_I = -P_N / \mathcal{J}_N, \quad (60)$$

$$X_K = -P_L / \mathcal{J}_N, \quad (61)$$

$$X_L = P_K / \mathcal{J}_N. \quad (62)$$

These results will be important to enforce the realizability constraints of the tensor impedance in terms of current coefficients only, as shown in Section V. Specifically, the square of the anisotropic component  $X_A$  becomes:

$$X_A^2 = X_K^2 + X_L^2 = \frac{P_K^2 + P_L^2}{\mathcal{J}_N^2}. \quad (63)$$

It is interesting to notice that another system can be derived from (47)–(54), if (47), (51) and (53) are chosen:

$$\begin{bmatrix} \mathcal{J}_I & \mathcal{J}_K & \mathcal{J}_L \\ \mathcal{J}_K & \mathcal{J}_I & 0 \\ \mathcal{J}_L & 0 & \mathcal{J}_I \end{bmatrix} \begin{bmatrix} X_I \\ X_K \\ X_L \end{bmatrix} = \begin{bmatrix} Q_I \\ Q_K \\ Q_L \end{bmatrix}. \quad (64)$$

Inverting (64), one obtains:

$$X_I = \frac{\mathcal{J}_I Q_I - \mathcal{J}_K Q_K - \mathcal{J}_L Q_L}{\mathcal{J}_I^2 - \mathcal{J}_K^2 - \mathcal{J}_L^2}, \quad (65)$$

$$X_K = \frac{-\mathcal{J}_K Q_I + \mathcal{J}_I Q_K + \mathcal{J}_L/\mathcal{J}_I(\mathcal{J}_K Q_L - \mathcal{J}_L Q_K)}{\mathcal{J}_I^2 - \mathcal{J}_K^2 - \mathcal{J}_L^2}, \quad (66)$$

$$X_L = \frac{-\mathcal{J}_L Q_I + \mathcal{J}_I Q_L + \mathcal{J}_K/\mathcal{J}_I(\mathcal{J}_L Q_K - \mathcal{J}_K Q_L)}{\mathcal{J}_I^2 - \mathcal{J}_K^2 - \mathcal{J}_L^2}. \quad (67)$$

These equations offer an alternative to (60)–(62) for the retrieval of  $X_I$ ,  $X_K$  and  $X_L$ ; however, they are not suitable for formulating the realizability constraints, since the numerators and denominators are *already* fourth-degree polynomials in the current coefficients (see Section V).

## V. ENFORCEMENT OF REALIZABILITY CONSTRAINTS

As explained in [32], [33], in order to exploit the advantages in terms of efficiency of a current-based optimization algorithm, all cost functionals must be expressed in terms of current coefficients only. Regarding the IBC constraints, the requirement for passivity and losslessness is maintained from the scalar version of the automated design method [32], [33], while new constraints must be introduced involving  $X_I$  and  $X_A$  (and their squares), as explained in Section III-B.

The enforcement of these constraints is based on the expression of the tensor impedance quantities in terms of the fields involved in the optimization process (the surface current  $\mathbf{J}$  and the tangential electric field  $\mathbf{E}_{\text{tan}}$ ). It is advantageous to limit the polynomial order of the functionals to four, which allows to limit the number of local minima and perform the line search in closed-form inside the nonlinear conjugate gradient algorithm [37].

Specifically, the realizability constraints aim at ensuring that the synthesizable impedance profile can be implemented using the chosen unit cell (e.g., the double-anchor geometry shown in Fig. 2). Recalling the feasibility region graphically represented in Figs. 5 and 6 and described in Section III-B, together with the quantities defined there, the impedance realizability constraints can be expressed as:

$$X_{\text{IL}} \leq X_I \leq X_{\text{IU}}, \quad X_{\text{IL}} < X_{\text{IU}} < 0, \quad (68)$$

$$A_L \leq X_A^2 \leq A_U, \quad A_U > A_L > 0, \quad (69)$$

$$X_A^2 \leq a_U X_I^2 + b_U X_I + c_U, \quad (70)$$

$$X_A^2 \geq a_L X_I^2 + b_L X_I + c_L. \quad (71)$$

Using (60), the constraints in (68) are equivalent to

$$X_{\text{IL}} + P_N/\mathcal{J}_N \leq 0 \implies X_{\text{IL}} \mathcal{J}_N^2 + P_N \mathcal{J}_N \leq 0, \quad (72)$$

$$-X_{\text{IU}} - P_N/\mathcal{J}_N \leq 0 \implies -X_{\text{IU}} \mathcal{J}_N^2 - P_N \mathcal{J}_N \leq 0, \quad (73)$$

while, employing (63), the ones in (69) become

$$A_L \mathcal{J}_N^2 - P_K^2 - P_L^2 \leq 0, \quad (74)$$

$$-A_U \mathcal{J}_N^2 + P_K^2 + P_L^2 \leq 0. \quad (75)$$

Finally, the constraints (70)–(71) can be written as

$$P_K^2 + P_L^2 - a_U P_N^2 + b_U P_N \mathcal{J}_N - c_U \mathcal{J}_N^2 \leq 0, \quad (76)$$

$$-P_K^2 - P_L^2 + a_L P_N^2 - b_L P_N \mathcal{J}_N + c_L \mathcal{J}_N^2 \leq 0. \quad (77)$$

These conditions are enforced in the average sense over each mesh cell. The impedance realizability cost function becomes:

$$\begin{aligned} f_{\text{IBC}} = & w_{\text{IL}}^{\text{imp}} \sum_i \rho_{\text{IL}i}^{\text{imp}} + w_{\text{IU}}^{\text{imp}} \sum_i \rho_{\text{IU}i}^{\text{imp}} \\ & + w_{\text{AL}}^{\text{imp}} \sum_i \rho_{\text{AL}i}^{\text{imp}} + w_{\text{AU}}^{\text{imp}} \sum_i \rho_{\text{AU}i}^{\text{imp}} \\ & + w_{\text{ML}}^{\text{imp}} \sum_i \rho_{\text{ML}i}^{\text{imp}} + w_{\text{MU}}^{\text{imp}} \sum_i \rho_{\text{MU}i}^{\text{imp}} \\ & + w^{\text{act}} \sum_i \rho_i^{\text{act}} \end{aligned} \quad (78)$$

where  $\rho_i^{\text{act}}$  represents the passivity and losslessness condition [32], [33],

$$\rho_i^{\text{act}} = P_i^2, \quad (79)$$

and the newly defined functionals are

$$\rho_{\text{IL}i}^{\text{imp}} = r(\Psi_{\text{IL}i}^{\text{imp}}), \quad \Psi_{\text{IL}i}^{\text{imp}} = P_{N_i} \mathcal{J}_{N_i} + X_{\text{IL}} \mathcal{J}_{N_i}^2, \quad (80)$$

$$\rho_{\text{IU}i}^{\text{imp}} = r(\Psi_{\text{IU}i}^{\text{imp}}), \quad \Psi_{\text{IU}i}^{\text{imp}} = -P_{N_i} \mathcal{J}_{N_i} - X_{\text{IU}} \mathcal{J}_{N_i}^2, \quad (81)$$

$$\rho_{\text{AL}i}^{\text{imp}} = r(\Psi_{\text{AL}i}^{\text{imp}}), \quad \Psi_{\text{AL}i}^{\text{imp}} = -P_{K_i}^2 - P_{L_i}^2 + A_L \mathcal{J}_{N_i}^2, \quad (82)$$

$$\rho_{\text{AU}i}^{\text{imp}} = r(\Psi_{\text{AU}i}^{\text{imp}}), \quad \Psi_{\text{AU}i}^{\text{imp}} = P_{K_i}^2 + P_{L_i}^2 - A_U \mathcal{J}_{N_i}^2, \quad (83)$$

$$\rho_{\text{ML}i}^{\text{imp}} = r(\Psi_{\text{ML}i}^{\text{imp}}), \quad (84)$$

$$\Psi_{\text{ML}i}^{\text{imp}} = -P_{K_i}^2 - P_{L_i}^2 + a_L P_{N_i}^2 - b_L P_{N_i} \mathcal{J}_{N_i} + c_L \mathcal{J}_{N_i}^2,$$

$$\rho_{\text{MU}i}^{\text{imp}} = r(\Psi_{\text{MU}i}^{\text{imp}}), \quad (85)$$

$$\Psi_{\text{MU}i}^{\text{imp}} = P_{K_i}^2 + P_{L_i}^2 - a_U P_{N_i}^2 + b_U P_{N_i} \mathcal{J}_{N_i} - c_U \mathcal{J}_{N_i}^2.$$

In the above,  $r(x) = \max(x, 0)$  is the ramp function. While the *squared* ramp function [32] has the advantage of being differentiable on the entire domain, it is not employed here because it would transform these functionals into eighth-degree polynomials in the current coefficients, thus hindering the computational efficiency of the line-search procedure [37], which is limited to fourth-degree polynomials. The weights  $w_{\text{IL}}^{\text{imp}}$ ,  $w_{\text{IU}}^{\text{imp}}$ ,  $w_{\text{AL}}^{\text{imp}}$ ,  $w_{\text{AU}}^{\text{imp}}$ ,  $w_{\text{ML}}^{\text{imp}}$ ,  $w_{\text{MU}}^{\text{imp}}$ ,  $w^{\text{act}}$ , together with the weights related to the radiation functionals and PEC condition (see Appendices A and B), have to be assigned a priori, like in all optimization problems of multiobjective nature; experience suggests to assign larger weights to the functionals enforcing impedance realizability, because they are harder to satisfy than the ones pertaining to the far-field masks. Introducing  $\mathbf{V} = \mathbf{G}^{-1}(\mathbf{V}_{\text{inc}} + \mathbf{L}\mathbf{l})$ , with  $\mathbf{G} \in \mathbb{R}^{N \times N}$  being the Gram matrix of the RWG basis functions, i.e.,

$$(\mathbf{G})_{mn} = \iint_{S_{\text{IBC}}} \mathbf{\Lambda}_m(\mathbf{r}) \cdot \mathbf{\Lambda}_n(\mathbf{r}) d\mathbf{r}, \quad (86)$$

the cell-wise terms appearing in the functionals above have the following expressions:

$$\mathcal{J}_{N_i} = \text{Im}(\mathbf{1}^H \mathbf{\Gamma}_{N_i}^i), \quad (87)$$

$$P_{T_i} = \text{Re}(\mathbf{1}^H \mathbf{\Gamma}_{T_i}^i \mathbf{V}), \quad T = N, K, L, \quad (88)$$

where  $\mathbf{\Gamma}_{T_i}^i \in \mathbb{R}^{N \times N}$ ,  $T = N, K, L$  is the (averaging) local *mixed* Gram matrix for the  $i$ -th cell, defined as

$$(\mathbf{\Gamma}_{T_i}^i)_{mn} = \frac{1}{A_i} \iint_{S_i} \mathbf{\Lambda}_m(\mathbf{r}) \cdot \overline{\mathbf{T}} \cdot \mathbf{\Lambda}_n(\mathbf{r}) d\mathbf{r}. \quad (89)$$

Given the large size of the problem, it is important that all gradients be formulated in such a way as to allow the use of fast algorithms and reduce the number of matrix-vector products [32]. Using the *complex gradient* operator, defined as [44]

$$\tilde{\nabla} f(\mathbf{z}) \equiv \frac{1}{2} (\nabla_x f(\mathbf{x}, \mathbf{y}) + j \nabla_y f(\mathbf{x}, \mathbf{y})), \quad (90)$$

where  $f(\mathbf{z}) = f(\mathbf{x}, \mathbf{y})$  is a real function of a complex vector variable  $\mathbf{z} = \mathbf{x} + j\mathbf{y} \in \mathbb{C}^N$ , the individual gradients of the newly defined functionals can be computed as:

$$\begin{aligned} \tilde{\nabla} \rho_{ILi}^{\text{imp}} = s(\Psi_{ILi}^{\text{imp}}) & \left[ 0.5 \mathcal{J}_{N_i} \boldsymbol{\nu}_{N_i} \right. \\ & - j (P_{N_i} + 2X_{IL} \mathcal{J}_{N_i}) \boldsymbol{\iota}_{N_i} \\ & \left. - 0.5 \mathcal{J}_{N_i} \mathbf{K}^H \boldsymbol{\iota}_{N_i} \right], \end{aligned} \quad (91)$$

$$\begin{aligned} \tilde{\nabla} \rho_{IUi}^{\text{imp}} = s(\Psi_{IUi}^{\text{imp}}) & \left[ -0.5 \mathcal{J}_{N_i} \boldsymbol{\nu}_{N_i} \right. \\ & + j (P_{N_i} + 2X_{IU} \mathcal{J}_{N_i}) \boldsymbol{\iota}_{N_i} \\ & \left. + 0.5 \mathcal{J}_{N_i} \mathbf{K}^H \boldsymbol{\iota}_{N_i} \right], \end{aligned} \quad (92)$$

$$\begin{aligned} \tilde{\nabla} \rho_{ALi}^{\text{imp}} = s(\Psi_{ALi}^{\text{imp}}) & \left[ -P_{K_i} \boldsymbol{\nu}_{K_i} - P_{L_i} \boldsymbol{\nu}_{L_i} \right. \\ & - 2j A_L \mathcal{J}_{N_i} \boldsymbol{\iota}_{N_i} \\ & \left. - \mathbf{K}^H (P_{K_i} \boldsymbol{\iota}_{K_i} + P_{L_i} \boldsymbol{\iota}_{L_i}) \right], \end{aligned} \quad (93)$$

$$\begin{aligned} \tilde{\nabla} \rho_{AUi}^{\text{imp}} = s(\Psi_{AUi}^{\text{imp}}) & \left[ P_{K_i} \boldsymbol{\nu}_{K_i} + P_{L_i} \boldsymbol{\nu}_{L_i} \right. \\ & + 2j A_U \mathcal{J}_{N_i} \boldsymbol{\iota}_{N_i} \\ & \left. + \mathbf{K}^H (P_{K_i} \boldsymbol{\iota}_{K_i} + P_{L_i} \boldsymbol{\iota}_{L_i}) \right], \end{aligned} \quad (94)$$

$$\begin{aligned} \tilde{\nabla} \rho_{MLi}^{\text{imp}} = s(\Psi_{MLi}^{\text{imp}}) & \left[ (a_L P_{N_i} - 0.5 b_L \mathcal{J}_{N_i}) \boldsymbol{\nu}_{N_i} - P_{K_i} \boldsymbol{\nu}_{K_i} \right. \\ & - P_{L_i} \boldsymbol{\nu}_{L_i} + j (b_L P_{N_i} - 2 c_L \mathcal{J}_{N_i}) \boldsymbol{\iota}_{N_i} \\ & \left. + \mathbf{K}^H \left( (-a_L P_{N_i} + 0.5 b_L \mathcal{J}_{N_i}) \boldsymbol{\iota}_{N_i} - P_{K_i} \boldsymbol{\iota}_{K_i} - P_{L_i} \boldsymbol{\iota}_{L_i} \right) \right], \end{aligned} \quad (95)$$

$$\begin{aligned} \tilde{\nabla} \rho_{MUi}^{\text{imp}} = s(\Psi_{MUi}^{\text{imp}}) & \left[ (-a_U P_{N_i} + 0.5 b_U \mathcal{J}_{N_i}) \boldsymbol{\nu}_{N_i} + P_{K_i} \boldsymbol{\nu}_{K_i} \right. \\ & + P_{L_i} \boldsymbol{\nu}_{L_i} - j (b_U P_{N_i} - 2 c_U \mathcal{J}_{N_i}) \boldsymbol{\iota}_{N_i} \\ & \left. + \mathbf{K}^H \left( (a_U P_{N_i} - 0.5 b_U \mathcal{J}_{N_i}) \boldsymbol{\iota}_{N_i} + P_{K_i} \boldsymbol{\iota}_{K_i} + P_{L_i} \boldsymbol{\iota}_{L_i} \right) \right]. \end{aligned} \quad (96)$$

In the above,  $s(x)$  is the Heaviside step function, and  $\mathbf{K} = \mathbf{G}^{-1} \mathbf{L}$ . The following cell-wise terms have been introduced:

$$\boldsymbol{\nu}_{T_i} = \mathbf{\Gamma}_{T_i}^i \mathbf{V}, \quad \boldsymbol{\iota}_{T_i} = \mathbf{\Gamma}_{T_i}^i \mathbf{1}, \quad T = N, K, L. \quad (97)$$

The total gradient is obtained by linearity as a sum of all individual gradients:

$$\begin{aligned} \tilde{\nabla} f_{\text{IBC}} = & w_{IL}^{\text{imp}} \sum_i \tilde{\nabla} \rho_{ILi}^{\text{imp}} + w_{IU}^{\text{imp}} \sum_i \tilde{\nabla} \rho_{IUi}^{\text{imp}} \\ & + w_{AL}^{\text{imp}} \sum_i \tilde{\nabla} \rho_{ALi}^{\text{imp}} + w_{AU}^{\text{imp}} \sum_i \tilde{\nabla} \rho_{AUi}^{\text{imp}} \\ & + w_{ML}^{\text{imp}} \sum_i \tilde{\nabla} \rho_{MLi}^{\text{imp}} + w_{MU}^{\text{imp}} \sum_i \tilde{\nabla} \rho_{MUi}^{\text{imp}} \\ & + w^{\text{act}} \sum_i \tilde{\nabla} \rho_i^{\text{act}}. \end{aligned} \quad (98)$$

The operator  $\mathbf{K}^H$  is interchanged with the summations in (98), thus allowing to compute the total gradient by requiring only one computationally intensive matrix-vector product [32]. The step function appearing in (91)–(96), due to the derivative of the first degree ramp function, causes the total gradient to be discontinuous, and this could be a potential issue for the convergence of the algorithm; however, in all the undertaken design cases, no problems were encountered during the synthesis process, demonstrating the robustness of the proposed method. The steps of the algorithm are summarized in Alg. 1.

## VI. FINAL LAYOUT: FIELD MATCHING UNIT CELL DESIGN

Whatever the design method involving the IBC, the final step in the realization of the metasurface is the determination of the unit cells that physically implement the synthesized impedance surface. At this stage, there is no longer a continuous spatial distribution of impedance  $\overline{\mathbf{Z}}(\mathbf{r})$ : the topology now is the *discrete* unit cell layout (most often, a square lattice). This means transforming the continuous impedance mapping  $\mathbf{r} \mapsto \overline{\mathbf{Z}}(\mathbf{r})$  into the discrete mapping  $\mathbf{r}_j \mapsto \overline{\mathbf{Z}}_j$ , where  $j$  indicates the cell with center  $\mathbf{r}_j$ ; this discretization is usually done by *sampling* the continuous profile, i.e.,  $\overline{\mathbf{Z}}_j = \overline{\mathbf{Z}}(\mathbf{r}_j)$ . The individual unit cells are then selected, from a precomputed database, based on their corresponding tensor impedance values (calculated using sheet impedance retrieval techniques for unit cells in a periodic environment, such as [11]); we will indicate with  $\mathcal{Z}_{\text{DB}} = \{\overline{\mathbf{z}}_p\}_{p=1}^P$  the set of impedance tensors in the database.

In this work, a novel strategy is devised to properly select the individual unit cells from the available database, that abandons the oversimplifying point sampling in the discretization of the surface impedance  $\overline{\mathbf{Z}}(\mathbf{r})$  leading to better antenna performances, especially for design instances in which the proposed numerical optimizer, while trying to satisfy the specified far-field masks and realizability constraints, does not converge to tensor impedance values within the imposed bounds everywhere on the surface.

Regarding the discretization of the surface, having established a priori the size of the unit cell that will be used to physically implement the synthesized tensor impedance, the triangular meshing of the radiating surface is done in such a way as to conform to the unit cell lattice; this simply means that an integer number of triangular mesh cells fits inside each unit cell. Therefore, for the designs tackled in this work, the impedance realizability constraints (80)–(85) are imposed in

**Algorithm 1** Algorithm for the design of the tensor impedance profile  $\bar{\mathbf{Z}}(\mathbf{r})$ .

---

**Input:**  $l_0, X_{IL}, X_{IU}, A_L, A_U, a_U, b_U, c_U, a_L, b_L, c_L,$   
 $\Omega_0, M_0, M_L^{co}, M_U^{co}, M^{cx}, M^{tot}$

**Output:**  $\mathbf{z}$

$l \leftarrow l_0$   
 $k \leftarrow 0$   
**while**  $k \leq K^{\max}$  **do**  
    Compute  $\mathcal{J}, \mathcal{J}_N, P, P_N, P_K, P_L$   $\triangleright$  (87)–(88)  
    Compute  $\rho^{\text{act}}, \rho_{IL}^{\text{imp}}, \rho_{IU}^{\text{imp}}, \rho_{AL}^{\text{imp}}, \rho_{AU}^{\text{imp}},$   $\triangleright$  (79)–(85)  
         $\rho_{ML}^{\text{imp}}, \rho_{MU}^{\text{imp}}$   
    Compute  $f_{\text{ibc}}$   $\triangleright$  (78)  
    Compute  $F_{\text{ref}}, F^{\text{co}}, F^{\text{cx}}, F^{\text{tot}}$   $\triangleright$  (106), (111)–(113)  
    Compute  $\rho_{\text{ref}}, \rho^{\text{co}}, \rho^{\text{cx}}, \rho^{\text{tot}}$   $\triangleright$  (105), (108)–(110)  
    Compute  $f_{\text{rad}}$   $\triangleright$  (104)  
    Compute  $f_{\text{pec}}$   $\triangleright$  (116)–(117) or (119)  
     $f \leftarrow f_{\text{ibc}} + f_{\text{rad}} + f_{\text{pec}}$   
    Compute  $\tilde{\nabla}\rho^{\text{act}}, \tilde{\nabla}\rho_{IL}^{\text{imp}}, \tilde{\nabla}\rho_{IU}^{\text{imp}}, \tilde{\nabla}\rho_{AL}^{\text{imp}},$   $\triangleright$  (91)–(96)  
         $\tilde{\nabla}\rho_{AU}^{\text{imp}}, \tilde{\nabla}\rho_{ML}^{\text{imp}}, \tilde{\nabla}\rho_{MU}^{\text{imp}}$   
    Compute  $\tilde{\nabla}f_{\text{ibc}}$   $\triangleright$  (98)  
    Compute  $\tilde{\nabla}\rho_{\text{ref}}, \tilde{\nabla}\rho^{\text{co}}, \tilde{\nabla}\rho^{\text{cx}}, \tilde{\nabla}\rho^{\text{tot}}$   $\triangleright$  see [32]  
    Compute  $\tilde{\nabla}f_{\text{rad}}$   
    Compute  $\tilde{\nabla}f_{\text{pec}}$   $\triangleright$  see [33]  
     $\tilde{\nabla}f \leftarrow \tilde{\nabla}f_{\text{ibc}} + \tilde{\nabla}f_{\text{rad}} + \tilde{\nabla}f_{\text{pec}}$   
    Set  $\beta_k$   $\triangleright$  see [32]  
    Set  $\mathbf{p}_k$   $\triangleright$  see [32]  
    Compute  $\alpha_k$   $\triangleright$  see [32]  
     $l_{k+1} \leftarrow l_k + \alpha_k \mathbf{p}_k$   
     $k \leftarrow k + 1$   
**end while**  
Compute  $\mathbf{z}$   $\triangleright$  (100)

---

an average sense over each *square cell*, and the synthesized tensor impedance components are retrieved through averaging over this same grid; we will call  $\mathbf{J}_j^{\text{opt,avg}}$  and  $\mathbf{E}_{\text{tan},j}^{\text{opt,avg}}$  these *average* values for the  $j$ -th cell, and  $\bar{\mathbf{Z}}_j^{\text{avg}}$  the impedance computed from the final current using (60)–(63).

1) *Cell design by impedance matching*: The usual selection process, that we will term “impedance matching”, retrieves the unit cell from the database as the one whose tensor impedance  $\bar{\mathbf{Z}}_j^*$  is the closest to  $\bar{\mathbf{Z}}_j^{\text{avg}}$ ,

$$\bar{\mathbf{Z}}_j^* = \arg \min_{\bar{\mathbf{z}} \in \mathcal{Z}_{\text{DB}}} \|\bar{\mathbf{z}} - \bar{\mathbf{Z}}_j^{\text{avg}}\|. \quad (99)$$

The norm (99) in the selection process can be defined in different manners; our choice is to define it in terms of the coefficients in the tensor basis  $\{\bar{\mathbf{I}}, \bar{\mathbf{K}}, \bar{\mathbf{L}}\}$ .

2) *Cell design by field matching*: One can observe that selecting an impedance tensor on the basis of the distance from the desired impedance *tensor* introduces an unnecessary restriction, namely that the relationship would work for *any* combination of the current and field values, while here the

optimal current is known, and so is the corresponding field (using (1)).

We now describe a new process to select the individual unit cells from a database. The selection is optimum for the specific computed optimal current; most significant is the fact that this new approach does *not require the determination of the impedance* from the optimized current. In fact, the optimal impedance tensor  $\bar{\mathbf{Z}}_j^*$  is found by selecting the impedance database entry that, when applied to  $\mathbf{J}_j^{\text{opt,avg}}$ , generates the field that best matches  $\mathbf{E}_{\text{tan},j}^{\text{opt,avg}}$ . In other words,

$$\bar{\mathbf{Z}}_j^* = \arg \min_{\bar{\mathbf{z}} \in \mathcal{Z}_{\text{DB}}} \|\mathbf{E}_{\text{tan},j}^{\text{opt,avg}} - \bar{\mathbf{z}} \cdot \mathbf{J}_j^{\text{opt,avg}}\|. \quad (100)$$

This strategy, from now on referred to as “field matching”, leads to superior performances, as described in the next section.

## VII. DESIGN EXAMPLES

The developed tensor design method has been applied to the design of (a) metasurface antennas with circular geometry of the radiating surface, and (b) a rectangular metasurface operating as anomalous reflector under an incident plane wave. For the circular antenna design, the feeder is placed at the center of the antenna; it consists of a vertical pin connected to the input coaxial cable, and an annular metal ring that provides matching to the surrounding surface. The feeder is designed separately to maximize guided wave coupling (see [33] and references therein). The 3-D source is represented by the equivalent magnetic currents located at the coaxial aperture in the ground plane, and the PEC condition is self-consistently enforced during the design on both the pin and the annular ring, as described in [33].

A RO3003 dielectric substrate with  $\epsilon_r = 3$  and thickness 1.27 mm is used throughout. With the exception of the initial test in Section VII-A, the circular antennas have a radius of  $12\lambda_0$  at the working frequency of 23 GHz, for a diameter of 312 mm; the rectangular metasurface is  $20\lambda_0$ -long and  $\lambda_0$ -wide at the same frequency, for an area of 260 mm  $\times$  13 mm. The structure in Section VII-A is a smaller circular antenna with a radius of  $6\lambda_0$ . For all circular antennas, we have employed the double-anchor unit cells with periodicity 1.625 mm, with impedance realizability constraints as listed in Section III-B; double anchors with  $w = 2.6$  mm are considered for the implementation of the rectangular metasurface.

The two circular antennas are designed with *linearly* polarized radiation patterns, specifically a pencil beam and a shaped cosecant beam. The design instances are carried out on a Desktop PC with Intel Core i9 processor and 64 GB RAM. The number of RWG basis functions for the full geometry is  $N = 87543$ , and the synthesis process for each antenna took around 1500 iterations, each requiring 18 s to complete, for a total running time of about 7 h 30 min for each design case.

The so-called “conversion efficiency” of these antennas will also be reported; it is computed as [45]

$$\epsilon_{\text{conv}} = \frac{P_{\text{rad}}}{P_{\text{in}}}, \quad (101)$$

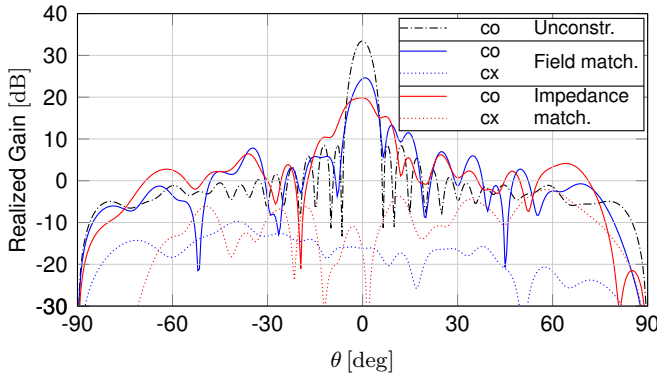


Fig. 7. Comparison of field matching and impedance matching unit cell designs, *unconstrained* test case of Section VII-A,  $\varphi = 0^\circ$  plane. The two approaches are applied to the current and field of the optimum solution; the radiation of the optimal current is labeled “unconstrained”, and compared with those of the solutions of the EFIE-IBC with impedance patterns obtained with the two approaches.

where  $P_{\text{rad}}$  is the radiated power and  $P_{\text{in}}$  is the net power accepted by the antenna from the connected feed. Since the calculated reflection coefficient is below  $-20$  dB for all these designs, approximately all of the input power available at the feed is accepted by the antenna. The conversion efficiency is used to estimate how much power remains trapped into the guided mode in the (infinite) substrate (zero for  $\epsilon_{\text{conv}} = 1$ ).

Finally, the rectangular metasurface is considered for designing an anomalous reflector that transforms a normal incident TE plane wave into a reflected TM wave towards  $(\theta_r, \varphi_r) = (40^\circ, 180^\circ)$ . The number of RWG basis functions for this geometry is  $N = 5790$ , and the optimization process took around 2000 iterations, each requiring 2s to complete, for a total running time of about 1 h.

In the following, apart from the unconstrained test case, all the far-field patterns referred to as “EFIE-IBC” are obtained by solving the EFIE-IBC (1) for the tensor impedance retrieved via field matching on the unit cell square lattice as explained in Section VI; for this reason, the impedance profile appears “pixelated”. In this way, the results take into account any possible efficiency reduction due to the impedance reconstruction process.

The final test is the full-wave solution of the actual layouts, where the IBC has been implemented with the proper double-anchor unit cells, using an in-house MoM solver. This solver employs the multilayer Green’s functions for infinite dielectric substrates [38] and uses a GIFFT algorithm [46], [47] to perform the matrix-vector products involving the EFIO operator (2). The corresponding far-field patterns will be referred to as “simulated”.

#### A. Unconstrained Design Test

The first design instance addresses the synthesis of a tensor metasurface antenna *without* enforcing the impedance realizability constraints, with the (obvious) exception of the passivity and losslessness condition; we will denote this as *unconstrained* design. In this example we consider a  $6\lambda_0$ -radius circular antenna that radiates a broadside linearly polarized

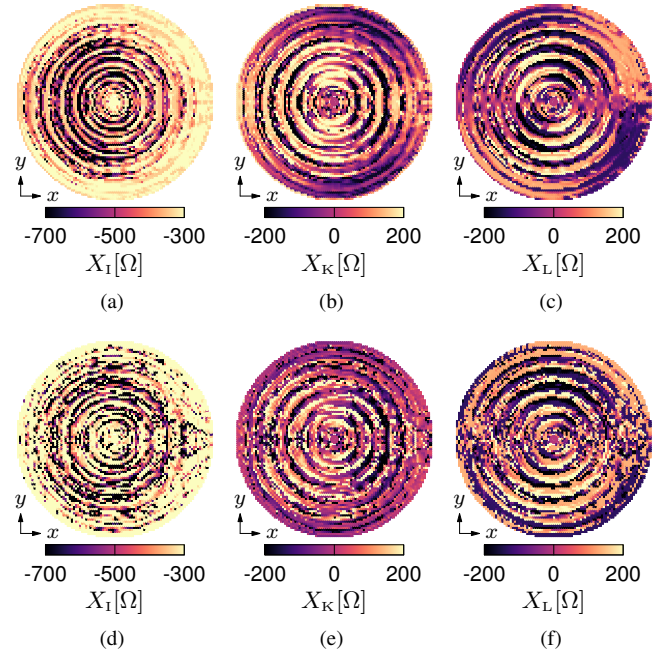


Fig. 8. *Unconstrained design*, tensor impedance components retrieved via field matching - (a),(b),(c), or impedance matching - (d),(e),(f).

(along  $\hat{x}$ ) pencil beam. Algorithmically, this is achieved by setting to zero the weights  $w_{\text{IL}}^{\text{imp}}$ ,  $w_{\text{IU}}^{\text{imp}}$ ,  $w_{\text{AL}}^{\text{imp}}$ ,  $w_{\text{AU}}^{\text{imp}}$ ,  $w_{\text{ML}}^{\text{imp}}$ ,  $w_{\text{MU}}^{\text{imp}}$  (see Section V).

We will denote by  $\mathbf{J}^{\text{opt}}(\mathbf{r})$  the current resulting from this unconstrained optimization instance. The cell-based impedance pattern  $\overline{\overline{\mathbf{Z}}}_j$  is obtained from the database of the double anchors in Section III-B via the field matching (FM) and impedance matching (IM) techniques of Section VI, resulting in the patterns  $\overline{\overline{\mathbf{Z}}}_j^{\text{FM}}$  and  $\overline{\overline{\mathbf{Z}}}_j^{\text{IM}}$ ; the EFIE-IBC (1) is then solved for these two tensor impedance patterns, yielding the currents  $\mathbf{J}^{\text{FM}}(\mathbf{r})$  and  $\mathbf{J}^{\text{IM}}(\mathbf{r})$ , respectively. Figure 7 shows the comparison between the field radiated by the current  $\mathbf{J}^{\text{opt}}(\mathbf{r})$  returned by the synthesis algorithm, and those generated by the currents  $\mathbf{J}^{\text{FM}}(\mathbf{r})$  and  $\mathbf{J}^{\text{IM}}(\mathbf{r})$  due to the two different unit cell impedance designs.

Overall, Fig. 7 shows that omission of impedance realizability constraints yields a solution that cannot be achieved as such with a given impedance database, as expected. Nonetheless, the field matching technique leads to a radiation pattern that preserves the shape of the broadside pencil beam, albeit with a lower gain and higher cross-polarization; this proves the robustness of this approach, and its optimality. Conversely, the impedance matching approach results in a drastic degradation of the main beam, with about 5 dB gain loss with respect to field matching, higher side lobes and worse cross-polarization.

Moreover, the field matching retrieval method also returns tensor impedance patterns with a much smoother profile than the ones obtained via impedance matching, as shown in Fig. 8. This is due to the fact that the field matching approach directly selects the appropriate unit cells based on the current and field on the surface (see Section VI-2) without computing the impedance profile from the optimal current. Indeed, the impedance recovery process may lead to localized “glitches”

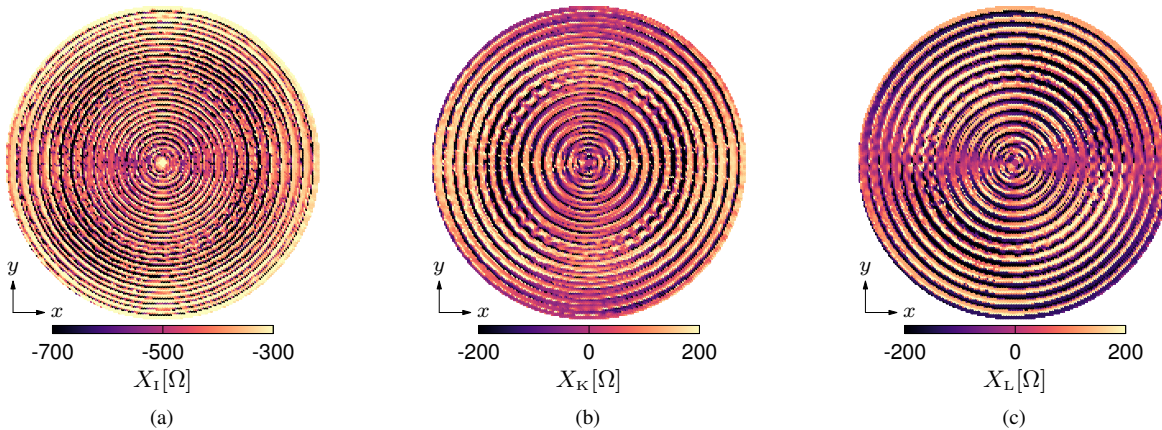


Fig. 9. *Linearly polarized pencil beam*, tensor impedance components: (a)  $X_I$ , (b)  $X_K$ , (c)  $X_L$ .

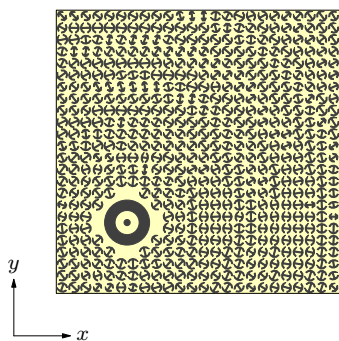


Fig. 10. *Linearly polarized pencil beam*: details of the implementation of the tensor impedance profile with double anchors around the central feed.

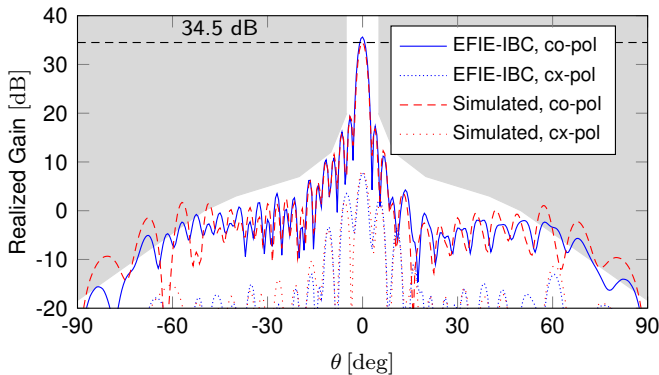


Fig. 11. *Linearly polarized pencil beam*, far-field cut at  $\varphi = 0^\circ$ : comparison between the simulated radiation pattern and the one obtained from the EFIE-IBC at the design stage.

that are totally avoided this way. It is also worth noticing that a more regular impedance profile allows for a better correspondence between IBC results and full-wave simulations, since the impedance database is computed within a periodic environment.

For these reasons, the field matching approach will be used for the selection of the unit cell impedances in all following designs.

TABLE II  
EFFICIENCIES OF MTS ANTENNAS RADIATING  
BROADSIDE PENCIL BEAMS.

| Ref.       | Pol.  | Radius          | $\epsilon_{\text{conv}}$ | $\epsilon_{\text{ap}}$ |
|------------|-------|-----------------|--------------------------|------------------------|
| [3]        | circ. | $13.5\lambda_0$ | 95%                      | 74%                    |
| [27]       | circ. | $12.5\lambda_0$ | 89.4%                    | 74.3%                  |
| This work* | circ. | $12\lambda_0$   | 96%                      | 71%                    |
| [2]        | lin.  | $10\lambda_0$   | N.R. <sup>†</sup>        | 54%                    |
| This work  | lin.  | $12\lambda_0$   | 88%                      | 74%                    |

\* Not shown in the paper.

† N.R.: not reported in the reference.

## B. Linearly Polarized Pencil Beam

We address now the design of an antenna with radius  $12\lambda_0$  radiating a linearly polarized pencil beam [2]. The tensor impedance components  $X_I$ ,  $X_K$ ,  $X_L$ , computed via field matching assuming  $(\hat{u}, \hat{v}) \equiv (\hat{x}, \hat{y})$ , are shown in Fig. 9. The synthesized tensor impedance profile is then physically implemented with double-anchor unit cells, employing the database of Section III-B with  $w = \lambda_0/8$ ; details of the double anchors around the center of the structure are shown in Fig. 10.

Finally, the far-field obtained with full-wave simulation of the actual antenna is shown in Fig. 11, together with ETSI Class 3 RPE [48] co-polarization mask (set on the whole 3-D upper hemisphere), and the far field returned by the EFIE-IBC at the design stage. From Fig. 11 it can be seen that the tensor metasurface designed with the proposed automated method generates a linearly polarized pencil beam with a *realized gain* of 34.5 dB, a conversion efficiency of 88% and an aperture efficiency equal to 74%. These values are equal or superior to the ones characterizing the MTS antennas reported in literature radiating broadside pencil beams [2], [3], [27], as shown in Table II. Linear polarization notoriously implies lower conversion efficiency with respect to circular, but we were unable to find a reference value in the literature; hence, in order to evaluate how the proposed synthesis method fares against other state-of-the-art techniques, the design of an antenna radiating a circularly polarized broadside beam is also carried out, and its performance metrics are added to Table II; its other results have been omitted for conciseness.

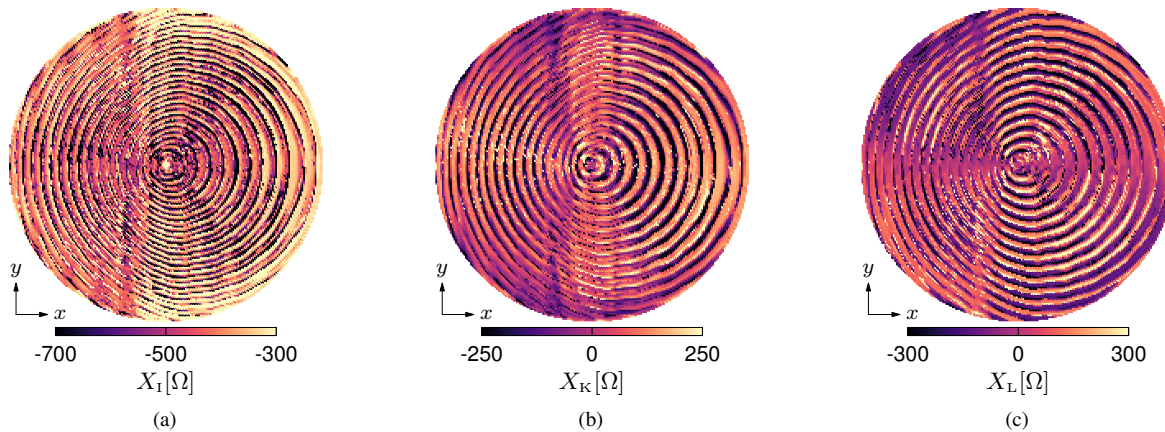


Fig. 12. *Linearly polarized cosecant squared pattern*, tensor impedance components: (a)  $X_I$ , (b)  $X_K$ , (c)  $X_L$ .

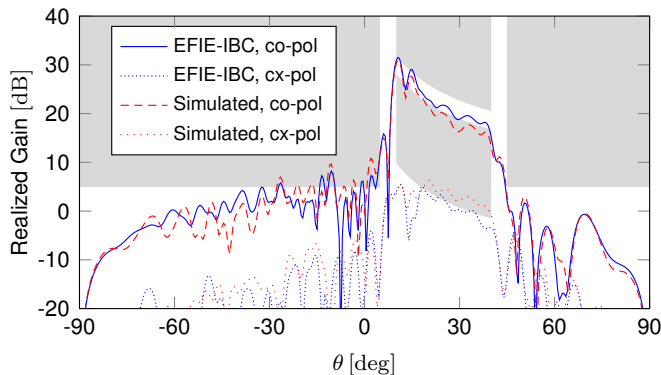


Fig. 13. *Linearly polarized cosecant squared pattern*, far-field cut at  $\varphi = 0^\circ$ : comparison between the simulated radiation pattern and the one obtained from the EFIE-IBC at the design stage.

### C. Linearly Polarized Cosecant Squared Pattern

The design of a tensor metasurface radiating a linearly polarized cosecant squared pattern [49] is addressed, with power pattern  $D(\theta)$  defined as [23], [32]

$$D(\theta) = \frac{\sin^2(\theta_{\min})}{\sin^2(\theta)}, \quad \theta_{\min} \leq \theta \leq \theta_{\max}. \quad (102)$$

In the considered case,  $\theta_{\min} = 10^\circ$ ,  $\theta_{\max} = 40^\circ$ , and the admissible ripple is set at  $\pm 2$  dB from the target mask. The tensor impedance components  $X_I$ ,  $X_K$ ,  $X_L$ , obtained using the proposed method without any a priori assumption on the impedance profile, are shown in Fig. 12, while the design and simulated radiation patterns are plotted in Fig. 13, appearing in very good agreement. While efficiency metrics for the linearly polarized cosecant squared pattern have not been found in literature, the conversion efficiency for this design is 92% and is higher than the values obtained in [25] for shaped beams with a specialized array feeder.

### D. Anomalous Reflection

Lastly, we target the design of a metasurface operating as an anomalous reflector: inspired by [50], the goal is to transform

a normal TE incident wave into a TM reflected wave towards  $(\theta_r, \varphi_r) = (40^\circ, 180^\circ)$ .

The tensor impedance components  $X_I$ ,  $X_K$ ,  $X_L$  synthesized with the proposed method are shown in Fig. 14, while the physical implementation using double-anchor unit cells with periodicity  $w = \lambda_0/5$  is pictured in Fig. 15. The choice of a larger unit cell with respect to previous designs is motivated by the need of mixed capacitive/inductive properties [50]. Finally, Fig. 16 shows the bistatic Radar Cross Section (RCS) [49], normalized to the total incident power on the metasurface, which is given by

$$P_{\text{inc}} = \frac{1}{2\eta_0} \cos \theta_i A, \quad (103)$$

where  $\eta_0$  is the free space intrinsic impedance,  $\theta_i$  is the angle of incidence and  $A$  is the metasurface area. The TM component of the RCS has a main beam directed towards  $(\theta_r, \varphi_r) = (40^\circ, 180^\circ)$ , as desired, with a magnitude 10 dB-larger than the backscattered TE wave at broadside. There is very good agreement between the results expected at the design stage and the ones obtained from full-wave simulation of the physical structure, the only difference being a slightly larger TM sidelobe towards  $\theta = 40^\circ$  in the latter.

## VIII. CONCLUSIONS AND FUTURE WORK

We have presented and validated an automatic, deterministic procedure for the complete design of tensor metasurfaces for field manipulation. The procedure takes as input the incident (feeding) field and the radiated field specifications, which are of the mask-type (inequalities). The design guarantees a passive and lossless metasurface. The tensor impedance pattern is allowed full spatial variability in two dimensions, without any assumption on the tensor components or spatial variation envelope, allowing designs otherwise difficult.

We have also presented two innovations that can be applied to general metasurface design methods, including those employing (meta-heuristic) global optimization of the impedance. The first is a compact representation of the impedance tensors that allows to enforce the synthesis of purely capacitive (or inductive) tensor impedances; furthermore, it allows to set independent bounds on the individual tensor components in

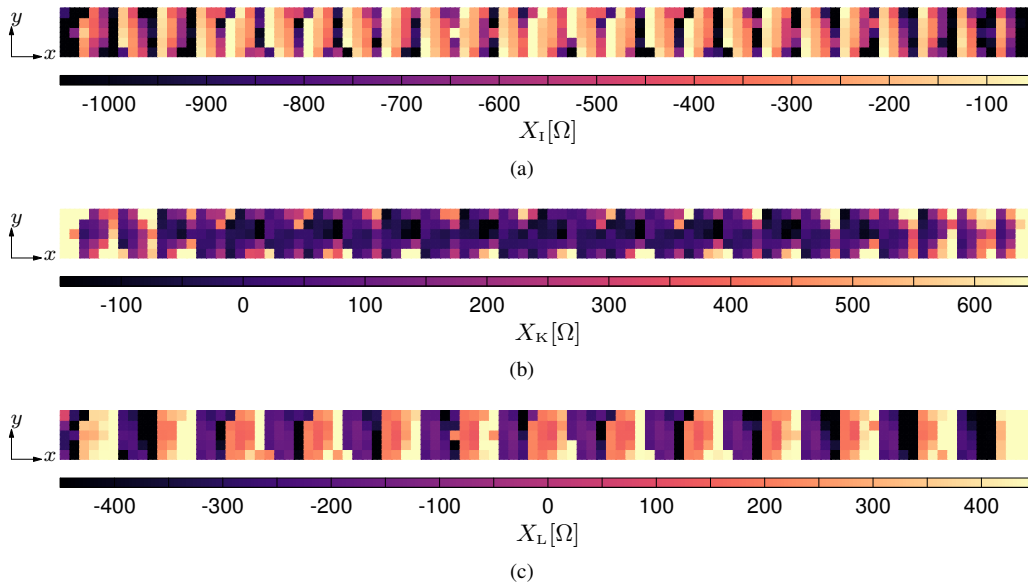


Fig. 14. *Anomalous reflection*, tensor impedance components: (a)  $X_I$ , (b)  $X_K$ , (c)  $X_L$ .



Fig. 15. *Anomalous reflection*: implementation of the tensor impedance profile with double-anchors.

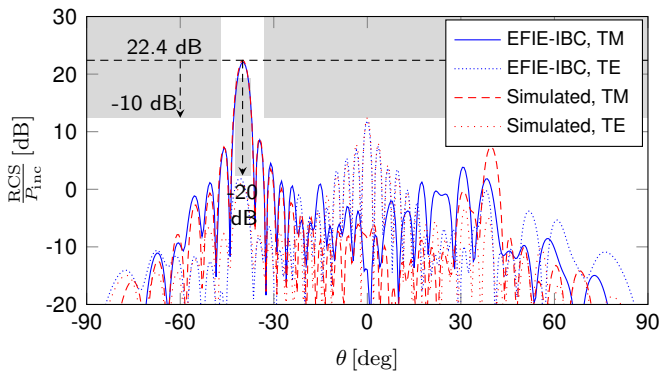


Fig. 16. *Anomalous reflection*, far-field cut at  $\varphi = 0^\circ$ : comparison between the simulated RCS and the one obtained from the EFIE-IBC at the design stage.

order to ensure the practical realizability of the designed structure. The second contribution concerns an innovative process to optimally choose the suitable unit cell shape from a database without the need to compute the impedance distribution.

Finally, the adopted formulation for the tensor impedance synthesis is well suited to systematically design a surface that can provide different radiation behaviors under different excitations; application to dual-polarization, multi-frequency, and beam switching is currently under way.

## APPENDIX A

### RADIATED FIELD FUNCTIONAL

The cost function encompassing the radiation requirements is defined as

$$f_{\text{rad}} = w^{\text{ref}} \rho^{\text{ref}} + w^{\text{co}} \rho^{\text{co}} + w^{\text{cx}} \rho^{\text{cx}} + w^{\text{tot}} \rho^{\text{tot}}, \quad (104)$$

where  $\rho^x$  and  $w^x$  (with “x” being “ref”, “co”, “cx” or “tot”) are the radiation functionals and their assigned weights, respectively. Specifically,

$$\rho_{\text{ref}} = r^2 (M_0 - F^{\text{ref}}) \quad (105)$$

enforces the desired minimum gain  $M_0$  with respect to the reference level  $F^{\text{ref}}$  evaluated in a small angular region  $\Omega_0$  around the maximum radiation direction  $\hat{r}_0$ ,

$$F_{\text{ref}} = \frac{1}{\Omega_0} \sum_{j \in \Omega_0} F_j^{\text{co}} \Delta\Omega_j \approx \frac{1}{N_0} \sum_{j \in \Omega_0} F_j^{\text{co}}. \quad (106)$$

The other functionals are given by the sum of terms over all considered far field directions:

$$\rho^x = \sum_{j=1}^{N_{\text{ff}}} \rho_j^x, \quad (107)$$

where “x” should be replaced by the corresponding component (“co”, “cx” or “tot”), and the index  $j = 1, \dots, N_{\text{ff}}$  refers to the far field direction  $(\theta_j, \phi_j)$ . Below are the definitions of each term:

$$\rho_j^{\text{co}} = r^2 (M_{L,j}^{\text{co}} - F_j^{\text{co}}) + r^2 (F_j^{\text{co}} - M_{U,j}^{\text{co}}), \quad (108)$$

$$\rho_j^{\text{cx}} = r^2 (F_j^{\text{cx}} - M_j^{\text{cx}}), \quad (109)$$

$$\rho_j^{\text{tot}} = r^2 (F_j^{\text{tot}} - M_j^{\text{tot}}). \quad (110)$$

In the above,  $M_{U,j}^{\text{co}}$  and  $M_{L,j}^{\text{co}}$  are the upper and lower masks on the co-polarization component, while  $M_j^{\text{cx}}$  and  $M_j^{\text{tot}}$  are the (upper) masks on the cross-polarization and on the sidelobes. Also,

$$F_j^{\text{co}} = |E_j^{\text{co}}|^2, \quad (111)$$

$$F_j^{\text{cx}} = |E_j^{\text{cx}}|^2, \quad (112)$$

$$F_j^{\text{tot}} = |E_j^{\text{co}}|^2 + |E_j^{\text{cx}}|^2, \quad (113)$$

where the co- and cross-polarization components of the electric field are obtained by applying the discretized radiation operator to the current coefficients:

$$\mathbf{E}^{\text{co}} = \mathbf{R}^{\text{co}} \mathbf{I}, \quad (114)$$

$$\mathbf{E}^{\text{cx}} = \mathbf{R}^{\text{cx}} \mathbf{I}. \quad (115)$$

### APPENDIX B PEC FUNCTIONAL

The PEC condition can be enforced either *cell-wise* or *edge-wise*. The *cell-wise* enforcement consists in minimizing the sum of the squares of fields on individual cells; the corresponding functional can be expressed as:

$$\rho^{\text{pec}} = \sum_{i \in \mathcal{I}_{\text{pec}}} \rho_i^{\text{pec}}, \quad (116)$$

with

$$\rho_i^{\text{pec}} = \frac{1}{A_i} \iint_{\mathcal{S}_i} |\mathbf{E}_{\text{tan}}|^2 dS. \quad (117)$$

Here,  $A_i$  is the surface area of  $\mathcal{S}_i$ , and  $\mathcal{I}_{\text{pec}} = \{i \in \mathbb{N} \mid \mathcal{S}_i \subset \mathcal{S}_{\text{PEC}}\}$  collects the indices of mesh cells belonging to the PEC region.

The *edge-wise* enforcement derives from considering explicitly the PEC condition in the discretized EFIE (PEC part of (1)):

$$\epsilon_{\text{pec}} = \mathbf{V}_{\text{pec}}^{\text{inc}} + \mathbf{L}_{\text{cpl}} \mathbf{l}_{\text{ibc}} + \mathbf{L}_{\text{pec}} \mathbf{l}_{\text{pec}} = 0. \quad (118)$$

In the above,  $\mathbf{L}_{\text{pec}}$  is the sub-matrix of (5) that represents the self-interaction on the PEC region,  $\mathbf{L}_{\text{cpl}}$  is the sub-matrix that encompasses the coupling between the IBC and PEC regions, and  $\mathbf{V}^{\text{inc}}$ ,  $\mathbf{l}$  with subscripts *ibc*, *pec* identify the sub-vectors of these quantities relative to the two regions.  $\epsilon_{\text{pec}}$  is the EFIE error, and its norm is the PEC-restricted EFIE residue that is minimized in the *edge-wise* version of the PEC functional:

$$\rho^{\text{pec}} = \|\epsilon_{\text{pec}}\|^2. \quad (119)$$

### APPENDIX C ENERGY AND IMPEDANCE TENSOR EIGENVALUES

Here, we derive the condition that the impedance must satisfy to ensure capacitive or inductive energy storage in terms of its eigenvalues. Starting from the definition of reactive energy for a surface current distribution,

$$w_e = \text{Im}(\mathbf{J}^* \cdot \mathbf{E}_{\text{tan}}), \quad (120)$$

substituting the IBC condition  $\mathbf{E}_{\text{tan}} = \overline{\overline{\mathbf{Z}}} \cdot \mathbf{J}$ , and considering a passive lossless impedance  $\overline{\overline{\mathbf{Z}}} = \mathbf{j} \overline{\overline{\mathbf{X}}}$ , we have

$$w_e = \text{Im}(\mathbf{J}^* \cdot \overline{\overline{\mathbf{Z}}} \cdot \mathbf{J}) = \text{Re}(\mathbf{J}^* \cdot \overline{\overline{\mathbf{X}}} \cdot \mathbf{J}). \quad (121)$$

We now recast the diagonalized version of the reactance tensor  $\overline{\overline{\mathbf{X}}}$  in terms of its eigenvectors  $\mathbf{u}_1, \mathbf{u}_2$ :

$$\overline{\overline{\mathbf{X}}} = \mathbf{u}_1 X_1 \mathbf{u}_1 + \mathbf{u}_2 X_2 \mathbf{u}_2. \quad (122)$$

Recalling that the eigenvectors and eigenvalues of  $\overline{\overline{\mathbf{X}}}$  are real, we have

$$w_e = |\mathbf{u}_1 \cdot \mathbf{J}|^2 X_1 + |\mathbf{u}_2 \cdot \mathbf{J}|^2 X_2. \quad (123)$$

The capacitive or inductive condition on the stored energy must hold for an arbitrary current  $\mathbf{J}$ , thus implying the condition on the sign of both eigenvalues

$$w_e \leq 0 \iff X_1 \leq 0 \text{ and } X_2 \leq 0. \quad (124)$$

### REFERENCES

- [1] G. Minatti, M. Faenzi, E. Martini, F. Caminita, P. De Vita, D. Gonzalez-Ovejero, M. Sabbadini, and S. Maci, "Modulated Metasurface Antennas for Space: Synthesis, Analysis and Realizations," *IEEE Trans. Antennas Propag.*, vol. 63, no. 4, pp. 1288–1300, Apr. 2015.
- [2] G. Minatti, F. Caminita, E. Martini, M. Sabbadini, and S. Maci, "Synthesis of Modulated-Metasurface Antennas With Amplitude, Phase, and Polarization Control," *IEEE Trans. Antennas Propag.*, vol. 64, no. 9, pp. 3907–3919, Sep. 2016.
- [3] M. Faenzi, G. Minatti, D. González-Ovejero, F. Caminita, E. Martini, C. Della Giovampaola, and S. Maci, "Metasurface Antennas: New Models, Applications and Realizations," *Scientific Reports*, vol. 9, no. 1, p. 10178, Dec. 2019.
- [4] E. Martini, M. Mencagli, D. Gonzalez-Ovejero, and S. Maci, "Flat Optics for Surface Waves," *IEEE Trans. Antennas Propag.*, vol. 64, no. 1, pp. 155–166, Jan. 2016.
- [5] M. Bosiljjevac, M. Casaletti, F. Caminita, Z. Sipus, and S. Maci, "Non-Uniform Metasurface Luneburg Lens Antenna Design," *IEEE Trans. Antennas Propag.*, vol. 60, no. 9, pp. 4065–4073, Sep. 2012.
- [6] J. Ruiz-García, E. Martini, C. D. Giovampaola, D. González-Ovejero, and S. Maci, "Reflecting Luneburg Lenses," *IEEE Trans. Antennas Propag.*, vol. 69, no. 7, pp. 3924–3935, Jul. 2021.
- [7] L. Szymanski, G. Gok, and A. Grbic, "Antenna Beamforming With Multiple-Input, Multiple-Output Metastructures: Controlling the Amplitude and Phase of Antenna Aperture Fields," *IEEE Antennas Propag. Mag.*, pp. 2–12, 2022.
- [8] B. B. Tierney, N. I. Limberopoulos, R. L. Ewing, and A. Grbic, "A Planar, Broadband, Metamaterial-Based, Transmission-Line Beamformer," *IEEE Trans. Antennas Propag.*, vol. 66, no. 9, pp. 4844–4853, Sep. 2018.
- [9] G. Oliveri, F. Zardi, P. Rocca, M. Salucci, and A. Massa, "Building a Smart EM Environment - AI-Enhanced Aperiodic Micro-Scale Design of Passive EM Skins," *IEEE Trans. Antennas Propag.*, vol. 70, no. 10, pp. 8757–8770, Oct. 2022.
- [10] G. Oliveri, F. Zardi, and A. Massa, "On the Improvement of the Performance of Inexpensive Electromagnetic Skins by Means of an Inverse Source Design Approach," *IEEE Trans. Antennas Propag.*, vol. 73, no. 5, pp. 3284–3295, May 2025.
- [11] A. M. Patel and A. Grbic, "Modeling and Analysis of Printed-Circuit Tensor Impedance Surfaces," *IEEE Trans. Antennas Propag.*, vol. 61, no. 1, pp. 211–220, Jan. 2013.
- [12] M. Teniou, H. Roussel, N. Capet, G.-P. Piau, and M. Casaletti, "Implementation of Radiating Aperture Field Distribution Using Tensorial Metasurfaces," *IEEE Trans. Antennas Propag.*, vol. 65, no. 11, pp. 5895–5907, Nov. 2017.
- [13] A. Epstein and G. V. Eleftheriades, "Synthesis of passive lossless metasurfaces using auxiliary fields for reflectionless beam splitting and perfect reflection," *Phys. Rev. Lett.*, vol. 117, no. 25, p. 256103, Dec. 2016.
- [14] D.-H. Kwon, "Modulated Reactance Surfaces for Leaky-Wave Radiation Based on Complete Aperture Field Synthesis," *IEEE Trans. Antennas Propag.*, vol. 68, no. 7, pp. 5463–5477, Jul. 2020.
- [15] V. G. Ataloglou and G. V. Eleftheriades, "Arbitrary Wave Transformations With Huygens' Metasurfaces Through Surface-Wave Optimization," *IEEE Antennas Wirel. Propag. Lett.*, vol. 20, no. 9, pp. 1750–1754, Sep. 2021.
- [16] J. Budhu and A. Grbic, "Perfectly Reflecting Metasurface Reflectarrays: Mutual Coupling Modeling Between Unique Elements Through Homogenization," *IEEE Trans. Antennas Propag.*, vol. 69, no. 1, pp. 122–134, Jan. 2021.
- [17] J. Budhu, E. Michielssen, and A. Grbic, "The Design of Dual Band Stacked Metasurfaces Using Integral Equations," *IEEE Trans. Antennas Propag.*, vol. 70, no. 6, pp. 4576–4588, Jun. 2022.
- [18] J. Budhu, L. Szymanski, and A. Grbic, "Design of Planar and Conformal, Passive, Lossless Metasurfaces That Beamform," *IEEE J. Microw.*, vol. 2, no. 3, pp. 401–418, Jul. 2022.
- [19] S. Pearson and S. V. Hum, "Optimization of Electromagnetic Metasurface Parameters Satisfying Far-Field Criteria," *IEEE Trans. Antennas Propag.*, vol. 70, no. 5, pp. 3477–3488, May 2022.

- [20] T. Brown, Y. Vahabzadeh, C. Caloz, and P. Mojabi, "Electromagnetic Inversion With Local Power Conservation for Metasurface Design," *IEEE Antennas Wirel. Propag. Lett.*, vol. 19, no. 8, pp. 1291–1295, Aug. 2020.
- [21] T. Brown and P. Mojabi, "Cascaded Metasurface Design Using Electromagnetic Inversion With Gradient-Based Optimization," *IEEE Trans. Antennas Propag.*, vol. 70, no. 3, pp. 2033–2045, Mar. 2022.
- [22] K. Achouri, M. A. Salem, and C. Caloz, "General Metasurface Synthesis Based on Susceptibility Tensors," *IEEE Trans. Antennas Propag.*, vol. 63, no. 7, pp. 2977–2991, Jul. 2015.
- [23] M. Bodehou, C. Craeye, E. Martini, and I. Huynen, "A Quasi-Direct Method for the Surface Impedance Design of Modulated Metasurface Antennas," *IEEE Trans. Antennas Propag.*, vol. 67, no. 1, pp. 24–36, Jan. 2019.
- [24] M. Bodehou, C. Craeye, and I. Huynen, "Electric Field Integral Equation-Based Synthesis of Elliptical-Domain Metasurface Antennas," *IEEE Trans. Antennas Propag.*, vol. 67, no. 2, pp. 1270–1274, Feb. 2019.
- [25] M. Bodehou and C. Craeye, "Array Surface-Wave Launcher for the Efficient Generation of Shaped Beam and Multibeam With Metasurface," *IEEE Trans. Antennas Propag.*, vol. 69, no. 12, pp. 8860–8865, Dec. 2021.
- [26] M. Bodehou, K. A. Khalifeh, S. N. Jha, and C. Craeye, "Direct Numerical Inversion Methods for the Design of Surface Wave-Based Metasurface Antennas: Fundamentals, Realizations, and Perspectives," *IEEE Antennas Propag. Mag.*, vol. 64, no. 4, pp. 24–36, Aug. 2022.
- [27] J. Cavillot, M. Bodehou, and C. Craeye, "Metasurface Antennas Design: Full-Wave Feeder Modeling and Far-Field Optimization," *IEEE Trans. Antennas Propag.*, vol. 71, no. 1, pp. 39–49, Jan. 2023.
- [28] J. Budhu, L. Szymanski, and A. Grbic, "Passive and Lossless, Closed Metasurfaces for Illusion Electromagnetics," in *2023 17th Eur. Conf. Antennas Propag. EuCAP*, Mar. 2023, pp. 1–5.
- [29] M. Salucci, A. Gelmini, G. Oliveri, N. Anselmi, and A. Massa, "Synthesis of Shaped Beam Reflectarrays With Constrained Geometry by Exploiting Nonradiating Surface Currents," *IEEE Trans. Antennas Propag.*, vol. 66, no. 11, pp. 5805–5817, Nov. 2018.
- [30] M. Salucci, G. Oliveri, and A. Massa, "An Innovative Inverse Source Approach for the Feasibility-Driven Design of Reflectarrays," *IEEE Trans. Antennas Propag.*, vol. 70, no. 7, pp. 5468–5480, Jul. 2022.
- [31] F. Verni, M. Righero, and G. Vecchi, "On the Use of Entire-Domain Basis Functions and Fast Factorizations for the Design of Modulated Metasurface," *IEEE Trans. Antennas Propag.*, vol. 68, no. 5, pp. 3824–3833, May 2020.
- [32] M. Zucchi, F. Verni, M. Righero, and G. Vecchi, "Current Based Automated Design of Realizable Metasurface Antennas With Arbitrary Pattern Constraints," *IEEE Trans. Antennas Propag.*, vol. 71, no. 6, pp. 4888–4902, Jun. 2023.
- [33] L. Teodorani, M. Zucchi, and G. Vecchi, "Generalized Deterministic Automated Design of Metasurface Antennas With 3-D Feeding Structures," *IEEE Trans. Antennas Propag.*, vol. 72, no. 11, pp. 8135–8150, Nov. 2024.
- [34] L. Teodorani, M. Zucchi, G. Giordanengo, R. Gaffoglio, and G. Vecchi, "Flexible Design of Broadside-Radiating Linearly-Polarized Edge-Fed Metasurface Antennas," *IEEE Access*, vol. 13, pp. 174922–174931, 2025.
- [35] L. Teodorani, M. Zucchi, and G. Vecchi, "Current-Based Design of Metasurface Antennas with Tensorial Surface Impedance," in *Proc. 19th Eur. Conf. Antennas Propag.*, Stockholm, Mar. 2025, pp. 487–490.
- [36] L. Teodorani, M. Zucchi, F. Lattanzio, and G. Vecchi, "Current-based design of tensor metasurfaces," in *2025 IEEE Antennas Propag. Soc. Int. Symp. AP-S/URSI*, Ottawa, Jul. 2025.
- [37] M. Zucchi, "Numerical Techniques for the Automated Design of Metasurface Antennas," Ph.D. dissertation, Politecnico di Torino, Oct. 2022.
- [38] K. A. Michalski and J. R. Mosig, "Multilayered media Green's functions in integral equation formulations," *IEEE Trans. Antennas Propag.*, vol. 45, no. 3, pp. 508–519, Mar. 1997.
- [39] S. Rao, D. Wilton, and A. Glisson, "Electromagnetic scattering by surfaces of arbitrary shape," *IEEE Trans. Antennas Propag.*, vol. 30, no. 3, pp. 409–418, May 1982.
- [40] K. A. Michalski, "Electromagnetic Field Computation in Planar Multilayers," in *Encyclopedia of RF and Microwave Engineering*. John Wiley & Sons, Ltd, 2005.
- [41] J. Nocedal and S. J. Wright, *Numerical Optimization*, 2nd ed., ser. Springer Series in Operations Research. New York: Springer, 2006.
- [42] I. Lindell, A. Sihvola, and I. Hänninen, "Perfectly anisotropic impedance boundary," *IET Microw. Antennas Propag.*, vol. 1, no. 3, p. 561, 2007.
- [43] J. G. V. Bladel, "Appendix 4: Dyadic Analysis," in *Electromagnetic Fields*. IEEE, 2007, pp. 1035–1042.
- [44] D. H. Brandwood, "A complex gradient operator and its application in adaptive array theory," *IEE Proc. H Microw. Opt. Antennas*, vol. 130, no. 1, pp. 11–16, Feb. 1983.
- [45] M. Bodehou, D. González-Ovejero, C. Craeye, S. Maci, I. Huynen, and E. Martini, "Power balance and efficiency of metasurface antennas," *Sci Rep*, vol. 10, no. 1, p. 17508, Oct. 2020.
- [46] Seung Mo Seo and Jin-Fa Lee, "A fast IE-FFT algorithm for solving PEC scattering problems," *IEEE Trans. Magn.*, vol. 41, no. 5, pp. 1476–1479, May 2005.
- [47] F. Fasenfest, Capolino, Wilton, Jackson, and Champagne, "A fast MoM solution for large arrays: Green's function interpolation with FFT," *IEEE Antennas Wirel. Propag. Lett.*, vol. 3, pp. 161–164, 2004.
- [48] "Fixed Radio Systems; Characteristics and requirements for point-to-point equipment and antennas; Part 4: Antennas," *EN 302 217-4 - V2.2.1*, Jul. 2025.
- [49] "IEEE Standard for Definitions of Terms for Antennas," *IEEE Std 145-2013 Revis. IEEE Std 145-1993*, pp. 1–50, Mar. 2014.
- [50] C. Yepes, M. Faenzi, S. Maci, and E. Martini, "Perfect non-specular reflection with polarization control by using a locally passive metasurface sheet on a grounded dielectric slab," *Appl. Phys. Lett.*, vol. 118, no. 23, p. 231601, Jun. 2021.

**Lucia Teodorani** (Member, IEEE) received the B.Sc. degree in Electronics Engineering for Energy and Information from the University of Bologna (Cesena campus), Cesena, Italy, in 2016, the M.Sc. degree in Electronics Engineering and the Ph.D. degree in Electrical, Electronics and Communication Engineering from Politecnico di Torino, Turin, Italy, in 2020 and 2024, respectively. In 2025, she joined the Department of Electronics and Telecommunications, Politecnico di Torino, as a postdoctoral researcher. Her research interests include advanced automated methods for the deterministic design of metasurface antennas and the development of fixed-frequency reconfigurable antennas employing lumped active components or liquid crystals.

**Marcello Zucchi** (Member, IEEE) received the B.Sc. degree in electronics and telecommunications engineering from the University of Bologna, Bologna, Italy, in 2014, the M.Sc. degree in electronics engineering and the Ph.D. in electrical, electronics and communications engineering from Politecnico di Torino, Turin, Italy, in 2018 and 2022, respectively. In 2023, he joined the Department of Electronics and Telecommunications, Politecnico di Torino, as a postdoctoral researcher. Since June 2025 he is a researcher in the Advanced Computing, Photonics & Electromagnetics (CPE) area at Fondazione LINKS, Turin. His research interests include global optimization algorithms for flat antenna design, automatic synthesis of metasurface antennas and field focusing algorithms for hyperthermia treatment.

**Giuseppe Vecchi** (Fellow, IEEE) received the Laurea and Ph.D. degrees in electronic engineering from the Politecnico di Torino, Turin, Italy, in 1985 and 1989, respectively, with doctoral research carried out partly at Polytechnic University, Farmingdale, NY, USA.

He was a Visiting Scientist with Polytechnic University of NY from 1989 to 1990. Since 1990, he has been with the Department of Electronics, Politecnico di Torino, as an Assistant Professor, an Associate Professor from 1992 to 2000, and a Professor since 2000. He was a Visiting Scientist with the University of Helsinki, Helsinki, Finland, in 1992, and has been an Adjunct Faculty with the Department of Electrical and Computer Engineering, University of Illinois at Chicago, Chicago, IL, USA, from 1997 to 2011. Since 2015, he has been serving as the Director of the Antenna and EMC Laboratory (LACE), Politecnico di Torino. His current research activities concern analytical and numerical techniques for design, measurement and diagnostics of antennas and devices, medical applications, and imaging.

Prof. Vecchi is a member of the Board of the European School of Antennas (ESOA) and the IEEE Antennas and Propagation Standard Committee. He has been an Associate Editor of the IEEE TRANSACTIONS ON ANTENNAS AND PROPAGATION, the Chairman of the IEEE AP/MTT/ED Italian joint Chapter, and a member of the IEEE-APS Educational Committee.